



HAL
open science

Wave propagation in random 2D turbulence: a multi-scale approach

Valentin Resseguier, Erwan Hascoët, Bertrand Chapron

► **To cite this version:**

Valentin Resseguier, Erwan Hascoët, Bertrand Chapron. Wave propagation in random 2D turbulence: a multi-scale approach. *Journal of Fluid Mechanics*, 2024, 997, pp.A51. 10.1017/jfm.2024.769 . hal-04549029v3

HAL Id: hal-04549029

<https://hal.science/hal-04549029v3>

Submitted on 22 Aug 2024

HAL is a multi-disciplinary open access archive for the deposit and dissemination of scientific research documents, whether they are published or not. The documents may come from teaching and research institutions in France or abroad, or from public or private research centers.

L'archive ouverte pluridisciplinaire **HAL**, est destinée au dépôt et à la diffusion de documents scientifiques de niveau recherche, publiés ou non, émanant des établissements d'enseignement et de recherche français ou étrangers, des laboratoires publics ou privés.

Banner appropriate to article type will appear here in typeset article

1 **Wave propagation in random 2D turbulence: a** 2 **multi-scale approach**

3 **Valentin Resseguier^{1,2†}, Erwan Hascoët³ and Bertrand Chapron⁴**

4 ¹INRAE, UR OPAALE, 17 avenue de Cucillé, F-35044 Rennes, France

5 ²LAB, SCALIAN DS, 2 Rue Antoine Becquerel, 35700 Rennes, France

6 ³Oceandatalab, 870 Rte de Deolen, 29280 Locmaria-Plouzané, France

7 ⁴LOPS, Ifremer, 1625 Rte de Sainte-Anne, 29280 Plouzané

8 (Received xx; revised xx; accepted xx)

9 To study two-dimensional dispersive waves propagating through turbulent flows, a new and
10 less restrictive fast waves approximation is proposed using a multiscale setting. In this ansatz,
11 large scale and small scale of the turbulence are treated differently. Correlation lengths of
12 the random small scale turbulence components can be considered negligible in the wave
13 packet propagating frame. Still, the large-scale flow can be relatively strong, to significantly
14 impact wavenumbers along the propagating rays. New theoretical results, numerical tools and
15 proxies are derived to describe ray and wave action distributions. All model parameters can
16 robustly be calibrated from the large-scale flow component only. We illustrate our purpose
17 with ocean surface gravity waves propagating in different types of surface currents. The
18 multiscale solution is demonstrated to efficiently document wave trapping effects by intense
19 jets.

20 **Key words:**

21 **MSC Codes** 76B15, 76M35, 82B31, 82C31, 37H10, 37L55

22 **1. Introduction**

23 This paper aims to revisit the ray-path concept for fast waves propagating over heterogeneous
24 turbulent flows. Considering ocean surface wave propagation, many authors have already
25 discussed the random changes of rays subject to a random current (Voronovich 1991; White
26 & Fornberg 1998; Smit & Janssen 2019), and consequences on wave action distributions.
27 Closures have been derived in the Eulerian setting (Bal & Chou 2002; Klyatskin & Koshel
28 2015; Borcea *et al.* 2019; Kafiabad *et al.* 2019; Bôas & Young 2020; Garnier *et al.*
29 2020). Some of these approaches can be traced back to wave-wave interactions models, e.g.
30 McComas & Bretherton (1977) (see also Kafiabad *et al.* 2019, and reference therein). In most

† Email address for correspondence: valentin.resseguier@inrae.fr

31 cases, the central assumption is either time-delta-correlated turbulent velocity (Voronovich
 32 1991; Klyatskin 2005; Klyatskin & Koshel 2015) and/or fast waves in comparison to fluid
 33 flow velocities (White & Fornberg 1998; Dysthe 2001; Bal & Chou 2002; Borcea *et al.* 2019;
 34 Kafiabad *et al.* 2019; Smit & Janssen 2019; Bôas & Young 2020; Garnier *et al.* 2020; Boury
 35 *et al.* 2023; Wang *et al.* 2023). Medium variations may be slow and delta-correlations are
 36 hardly justifiable in a fixed frame. Though, attached to a fast propagating wave group, the
 37 medium may seem to vary rapidly, and the delta-correlation assumption makes more sense.
 38 Another common assumption is frozen turbulence. In such a case, weak currents also implies
 39 conservation along ray of intrinsic frequency, wavenumber, and group velocity magnitude
 40 in two dimension (Boury *et al.* 2023). Subsequently, most of wave dynamics models neglect
 41 variations and diffusion of frequency or wavenumber.

42 The diffusion of the wave action at large distance with a multiscale decomposition of the
 43 current has already been reported (Bal & Chou 2002). However, an explicit formulation for
 44 the diffusivity has solely been derived for a zero large-scale current. More generally, fast
 45 wave models mostly rely either on zero or constant current components at larger scales. West
 46 (1978), for instance, discussed acoustic waves in a two-component random media, but no
 47 velocity was involved.

48 Hereafter, the proposed two-scale velocity decomposition falls into the family of stochastic
 49 transport models (Kunita 1997; Mikulevicius & Rozovskii 2004; Resseguier *et al.* 2020a;
 50 Zhen *et al.* 2023), including dynamics under Location Uncertainty (LU) (Mémmin 2014;
 51 Resseguier *et al.* 2017a) and Stochastic Advection by Lie Transport (SALT) (Holm 2015).
 52 Under this framework, the small-scale velocity component is delta-correlated in time (Cotter
 53 *et al.* 2017). Up to usual source terms, fluid dynamics quantities (temperature, momentum,
 54 etc) are transported by both the large-scale revolved component and that random unresolved
 55 turbulence component. The stochastic closures obtained are conservative. Nonlinear wave
 56 Hamiltonian dynamics and wave influence on currents (e.g. stokes drift) have then been
 57 derived (e.g. Crisan & Holm 2018; Bauer *et al.* 2020; Holm 2021; Holm & Luesink
 58 2021; Dinvey & Mémmin 2022; Holm *et al.* 2023). Considering a single-wavevector current,
 59 solutions for a monochromatic shallow water wave were developed by Mémmin *et al.* (2022).
 60 In the present study, our objective is restricted to the influence of turbulent flows on linear
 61 waves.

62 After first recalling the principles of the ray tracing method, we present the multiscale
 63 framework for fast wave dynamics, its physical grounds and a calibration method for the
 64 closure. Simplified stochastic equations are then derived for the ray dynamics and the
 65 wave action spectrum, in both Lagrangian and Eulerian settings. For illustrative examples,
 66 numerical tools, analytic models and proxies are applied to ocean surface gravity waves
 67 propagating through two types of 2D turbulent flows: a typical slow homogeneous turbulence
 68 and a jet case.

69 2. Characteristics of wave-packet rays

70 Isolating a single progressive group of quasi-regular wave train, it follows a form
 71 $h(\mathbf{x}, t)e^{i\phi(\mathbf{x}, t)} + \text{c.c.}$, for most properties. Typically, h would be the local wave height with
 72 meters units. If a packet is to be followed, the phase, $\phi(\mathbf{x}, t)$, must smoothly vary along the
 73 propagation, i.e. $\phi(\mathbf{x}, t)$ is differentiable. The relative frequency is then $\omega = -\partial_t \phi(\mathbf{x}, t)$, and
 74 the wave number vector $\mathbf{k} = \nabla \phi(\mathbf{x}, t)$, with wavenumber $k = \|\mathbf{k}\|$ and direction given by
 75 the normalized wave-vector, $\tilde{\mathbf{k}} = \mathbf{k}/k = \begin{pmatrix} \cos \theta_k \\ \sin \theta_k \end{pmatrix}$. To first order, such a train of waves is

76 dispersive and the intrinsic frequency reads

$$77 \quad \omega - \mathbf{k} \cdot \mathbf{v} = \omega_0 = \begin{cases} \text{cst. } \frac{1}{\alpha} k^\alpha, & \alpha \neq 0 \\ \text{cst. } \log(k), & \alpha = 0 \end{cases} \quad (2.1)$$

78 and propagates with its group velocity $\mathbf{v}_g = \nabla_{\mathbf{k}} \omega$, constantly modified by the local velocity
79 of the currents \mathbf{v} ,

$$80 \quad \frac{d\mathbf{x}_r}{dt} = \mathbf{v}_g = \mathbf{v}_g^0 + \mathbf{v}, \quad (2.2)$$

81 where \mathbf{x}_r is the centroid of a wave group, $\mathbf{v}_g^0 = \frac{\partial \omega_0(k)}{\partial \mathbf{k}} \tilde{\mathbf{k}}$ is the group velocity without
82 currents, i.e. solely depending on the wave vector. For $\alpha = 1$, the medium is non-dispersive
83 (e.g. acoustic waves). $\alpha = 1/2$ corresponds to gravity waves over deep ocean ($\omega_0 = \sqrt{gk}$).
84 The dominant wave-vector \mathbf{k} within the group evolves according to

$$85 \quad \frac{d\mathbf{k}}{dt} = -\nabla_{\mathbf{v}} \mathbf{v}^T \mathbf{k}. \quad (2.3)$$

86 Equations (2.2)-(2.3) are the Hamilton's eikonal equations. Along the propagating ray,
87 velocity gradients induce linear variations. Decelerating currents will, for instance, shorten
88 waves, and reduce the group velocity. Traveling over fields of random velocities \mathbf{v} , the wave-
89 vector \mathbf{k} will also become randomly distributed. Scattering of ocean surface wave packets
90 by random currents can generally be assumed to be weak, with $\|\mathbf{v}\|$ of order $0.5 \text{ m}\cdot\text{s}^{-1}$,
91 much smaller than $v_g^0 = \|\mathbf{v}_g^0\|$ of order $10 \text{ m}\cdot\text{s}^{-1}$. Yet, cumulative effects of these random
92 surface currents can lead to strong convergence or divergence between initially nearby ray
93 trajectories.

94 To complete the wave field description, $E(\mathbf{x}, t) = \frac{1}{2} \rho g h^2(\mathbf{x}, t)$ and $A(\mathbf{x}, t) =$
95 $E(\mathbf{x}, t) / \omega_0(k(\mathbf{x}, t))$ denote energy and action by unit of surface. E is expressed in
96 J/m^2 and A in $J\cdot s/m^2$. To avoid spurious notations, we set the multiplicative constant $\frac{1}{2} \rho g$
97 to unity. The wave action is considered to be an adiabatic invariant in absence of source
98 terms. Wave action is then crucial to anticipate wave transformations by currents (White
99 1999). Unlike wave energy, wave action is conserved, in the absence of wave generation or
100 dissipation. This action is the integral over wave-vectors of the action spectrum, N , also
101 related to the wave energy spectrum, E :

$$102 \quad A(\mathbf{x}, t) = \int d\mathbf{k} N(\mathbf{x}, \mathbf{k}, t) = \int d\mathbf{k} \frac{E(\mathbf{x}, \mathbf{k}, t)}{\omega_0(\mathbf{k}, t)}. \quad (2.4)$$

103 Action and energy spectrum quantify action and energy by unit of surface (unit of \mathbf{x}) and by
104 unit of wave-vector surface (unit of \mathbf{k}). Consider the (\mathbf{x}, \mathbf{k}) variable change between different
105 times t_i and t_f integrating the characteristic eikonal equations (2.2)-(2.3)

$$106 \quad \begin{pmatrix} \mathbf{x}_r(t_i) \\ \mathbf{k}(t_i) \end{pmatrix} \mapsto \begin{pmatrix} \mathbf{x}_r(t_f) \\ \mathbf{k}(t_f) \end{pmatrix}. \quad (2.5)$$

107 According to the Liouville theorem for Hamiltonian mechanics (Landau & Lifshits 1960,
108 §46), the state-space of the "packet-by-packet" approach (the (\mathbf{x}, \mathbf{k}) space) does not contract
109 nor dilates along time. Readers not familiar with Hamiltonian dynamics may see the
110 divergence free of the 4-dimensional flow (2.5) – i.e. $\nabla_{\mathbf{x}} \cdot \frac{d\mathbf{x}_r}{dt} + \nabla_{\mathbf{k}} \cdot \frac{d\mathbf{k}}{dt} = 0$ – as the
111 divergence free of incompressible flow velocities, leading naturally to volume-preserving
112 dynamics. Therefore, if wave dissipation is neglected, the wave action spectrum N is
113 conserved (Lavrenov (2013)), i.e.

$$114 \quad N(\mathbf{x}_r(t_i), \mathbf{k}(t_i), t_i) = N(\mathbf{x}_r(t_f), \mathbf{k}(t_f), t_f). \quad (2.6)$$

115 This result is extremely useful because it only involves quantities of the characteristics, i.e.
 116 each Fourier mode can be modified independently of the others. The wave energy spectrum
 117 can be computed from the characteristics

$$118 \quad E(\mathbf{x}_r(t_f), \mathbf{k}(t_f), t_f) = \frac{\omega_0(\mathbf{k}(t_f))}{\omega_0(\mathbf{k}(t_i))} E(\mathbf{x}_r(t_i), \mathbf{k}(t_i), t_i). \quad (2.7)$$

119 starting with an initial incoming wave spectrum $E(\mathbf{x}_r(t_i), \mathbf{k}(t_i), t_i)$ for every wave-vectors
 120 $\mathbf{k}(t_i)$, starting from a small set of spatial points $\mathbf{x}_r(t_i)$.

121 3. A new fast wave assumption

122 Eikonal equations (2.2)-(2.3) are driven by currents and their gradients. Commonly, the
 123 Eulerian current \mathbf{v} is decomposed into a low-frequency large-scale component $\bar{\mathbf{v}}$ and a
 124 transient small-scale unresolved component \mathbf{v}' :

$$125 \quad \mathbf{v} = \bar{\mathbf{v}} + \mathbf{v}'. \quad (3.1)$$

126 Current gradients naturally follow the same scale separation. From now on, we shall consider
 127 divergence-free two-dimensional currents only.

128 3.1. The ray Lagrangian correlation time

129 To better characterize the wave dynamics in such a random environment, the covariance of the
 130 fluid velocity can be evaluated in the wave group frame. To take into account the small-scale
 131 unresolved component \mathbf{v}' , its Eulerian spatio-temporal covariance is considered, assuming
 132 statistical homogeneity and stationarity for the Eulerian velocity $\mathbf{v}'_E(t, \mathbf{x}) = \mathbf{v}'(t, \mathbf{x})$

$$133 \quad C_{ij}^{v'_E}(\delta t, \delta \mathbf{x}) = \mathbb{E} \left(v'_i(t, \mathbf{x}) v'_j(t + \delta t, \mathbf{x} + \delta \mathbf{x}) \right) = \mathbb{E} \left(v'_i(t, \mathbf{x}_r(t)) v'_j(t + \delta t, \mathbf{x}_r(t) + \delta \mathbf{x}) \right) \quad (3.2)$$

134 where \mathbf{x}_r is solution of (2.2) with an arbitrary initial position \mathbf{x}_r^0 . Then, we define, $v'_R(t) =$
 135 $v'(t, \mathbf{x}_r(t))$, the Lagrangian velocity along the ray $\mathbf{x}_r(t)$. The temporal covariance of the
 136 small-scale component \mathbf{v}' – in the wave group frame – is the covariance of that Lagrangian
 velocity:

$$137 \quad C_{ij}^{v'_R}(\delta t) = \mathbb{E} \left(v'_i(t, \mathbf{x}_r(t)) v'_j(t + \delta t, \mathbf{x}_r(t + \delta t)) \right) = C_{ij}^{v'_E}(\delta t, \mathbf{x}_r(t + \delta t) - \mathbf{x}_r(t)), \quad (3.3)$$

138 Assume for example a typical isotropic form for the Eulerian covariance:

$$139 \quad C^{v'_E}(\delta t, \delta \mathbf{x}) = C \left(\frac{|\delta t|}{\tau_{v'}} + \frac{\|\delta \mathbf{x}\|}{l_{v'}} \right), \quad (3.4)$$

140 the covariance can be evaluated in the wave group frame for small time increment δt :

$$141 \quad C^{v'_R}(\delta t) = C \left(\frac{|\delta t|}{\tau_{v'}} + \frac{\|\mathbf{x}_r(t' + t) - \mathbf{x}_r(t')\|}{l_{v'}} \right) = C \left(\left(\frac{1}{\tau_{v'}} + \frac{\|\mathbf{v}_g\|}{l_{v'}} \right) |\delta t| + O(\delta t^2) \right), \quad (3.5)$$

142 since $\mathbf{x}_r(t' + t) - \mathbf{x}_r(t') = \mathbf{v}_g \delta t + O(\delta t^2)$. Therefore, $\left(\frac{1}{\tau_{v'}} + \frac{\|\mathbf{v}_g\|}{l_{v'}} \right)^{-1}$ is the correlation time
 143 of $\mathbf{v}'(t, \mathbf{x}_r(t))$. For fast waves, the along-ray correlation time of the small-scale velocity can
 144 be approximated by $l_{v'}/v_g^0$. Note that eikonal equations (2.2)-(2.3) involve both velocity and
 145 velocity gradients. The above derivation is also valid for the small-scale velocity gradients
 146 $(\nabla \mathbf{v}')'(t, \mathbf{x}_r(t))$. The ratio ϵ , between that along-ray correlation time and the characteristic
 147 time of the wave group properties evolution, will then control the time decorrelation

148 assumption of \mathbf{v}' :

$$149 \quad \epsilon = \frac{l_{v'}}{v_g^0} \|\nabla \mathbf{v}'\| \sim \frac{l_{v'}}{l_v} \frac{\|\mathbf{v}'\|}{v_g^0}. \quad (3.6)$$

150 This time scale estimation can be obtained from spatio-temporal covariances more general
151 than (3.4) (not shown) even though the derivation is more technical. Note the Eulerian small-
152 scale velocity \mathbf{v}' is not necessarily time uncorrelated, as assumed in Voronovich (1991);
153 Klyatskin & Koshel (2015). Yet, for small enough ϵ , the Lagrangian small-scale velocity
154 along the ray can be considered time uncorrelated. From the expression of ϵ , such a condition
155 depends upon:

- 156 • v_g^0 , the fast wave group velocity
- 157 • $\|\mathbf{v}'\|$, often slow but not always negligible compared to the intrinsic wave group, v_g^0 .
- 158 • $l_{v'}/l_v$, related to the separation between large scales $\bar{\mathbf{v}}$ and small scales \mathbf{v}' , e.g. the
159 spatial filtering cutoff of the large-scale velocity $\bar{\mathbf{v}}$, but also related to its kinetic energy (KE)
160 distribution over spatial scales, typically the spectrum slope.

161 This along-ray partial time-decorrelation assumption is less restrictive than the usual fast
162 wave approximation (White & Fornberg 1998; Dysthe 2001; Bal & Chou 2002; Borcea
163 *et al.* 2019; Kafiabad *et al.* 2019; Smit & Janssen 2019; Bôas & Young 2020; Garnier *et al.*
164 2020; Boury *et al.* 2023; Wang *et al.* 2023) – say $\frac{\|\mathbf{v}'\|}{v_g^0} \ll 1$ – and than the SALT-LU time-
165 decorrelation used for turbulence dynamics (Mémin 2014; Holm 2015; Cotter *et al.* 2017;
166 Resseguier *et al.* 2020a) – say $\frac{l_{v'}}{l_v} \ll 1$. Similarly, this last validity criterion can be obtained
167 replacing in (3.2)-(3.6) \mathbf{x}_r by the fluid particle Lagrangian path \mathbf{x} (solution of $\frac{d\mathbf{x}}{dt} = \mathbf{v}$)
168 and thus v_g^0 by v . These asymptotic models often rely on averaging or homogenization
169 techniques (Papanicolaou & Kohler 1974; White & Fornberg 1998) to derive Markovian
170 dynamics involving various types of diffusivity.

171 3.2. Ray absolute diffusivity and turbulence statistics: calibration

172 Diffusivity is a natural tool to specify statistics of uncorrelated random media. For waves in
173 random media, we shall specify multi-point statistics, and the Fourier space is convenient for
174 this purpose. We will first present scalar diffusivity and then distribute it over spatial scales to
175 fully calibrate the random velocity \mathbf{v}' , i.e. choose some parameter values to set the statistics
176 of that velocity field. As such, we will obtain a closed model to derive analytic results and
177 generate samples for simulations.

178 The absolute diffusivity (or Kubo-type formula) usually corresponds, in the so-called
179 diffusive regime, to the variance per unit of time of a fluid particle Lagrangian path $\frac{d\mathbf{x}(t)}{dt} =$
180 $\mathbf{v}_L(t) = \mathbf{v}(t, \mathbf{x}(t))$. It is approximately equal to the velocity variance times its correlation time.
181 The Eulerian velocity covariance (3.4) will thus induce an absolute diffusivity (Piterbarg &
182 Ostrovskii 1997; Klyatskin 2005)

$$183 \quad \frac{1}{2}a^L = \int_0^{+\infty} d\delta t C^{v'_L}(\delta t) = \int_0^{+\infty} d\delta t C^{v'_E}(\delta t, \mathbf{x}(t + \delta t) - \mathbf{x}(t)) \approx \frac{1}{2}\tau_{v'} C(0). \quad (3.7)$$

184 This diffusivity well describes effects of fast-varying eddies but is not appropriate in our case.
185 Indeed, along a propagating wave group, $\frac{d\mathbf{x}_r(t)}{dt} = \mathbf{v}_g^0(t) + \mathbf{v}_R(t)$, a ray absolute diffusivity
186 occurs and slightly differs from the usual absolute diffusivity to become

$$187 \quad \frac{1}{2}a^R = \int_0^{+\infty} d\delta t C^{v'_R}(\delta t) \approx \frac{1}{2} \left(\frac{1}{\tau_{v'}} + \frac{\|\mathbf{v}_g^0\|}{l_{v'}} \right)^{-1} C(0) \approx \frac{1}{2} \frac{l_{v'}}{v_g^0} C(0). \quad (3.8)$$

188 The absolute diffusivity sets the amplitude of the small scale velocity \mathbf{v}' . Indeed, since the

189 kinetic energy of a time-continuous white noise is infinite, it has no physical meaning. It is
 190 more relevant to deal with absolute diffusivity rather than kinetic energy in order to describe
 191 the statistics of the time-uncorrelated velocity. To calibrate its spatial correlations, we may
 192 focus on its Fourier transform, $\widehat{\mathbf{v}'}(\boldsymbol{\kappa}, t)$, denoting by $\boldsymbol{\kappa} = \kappa \begin{pmatrix} \cos \theta_\kappa \\ \sin \theta_\kappa \end{pmatrix}$, the surface current
 193 wave-vector. By analogy with the current kinetic energy spectra $E_\kappa = \frac{1}{2} \oint_0^{2\pi} d\theta_\kappa \kappa \frac{\|\widehat{\mathbf{v}'}(\boldsymbol{\kappa}, t)\|^2}{(2\pi)^2}$,
 194 Resseguier *et al.* (2017b, 2020b) decompose the absolute diffusivity scale by scale:

$$195 \quad a^R = \int_0^{+\infty} A_{\mathbf{v}'}^R(\kappa) d\kappa. \quad (3.9)$$

196 Referring it to Absolute Diffusivity Spectral Density (ADSD), it is defined as the kinetic
 197 energy spectra multiplied by the correlation time at each scale, $\tau(\kappa)$. Unlike Resseguier *et al.*
 198 (2017b, 2020b), that correlation time is here imposed by the wave dynamics. Therefore, by
 199 analogy with (3.8) we choose a correlation time $\tau^R(\kappa) = \frac{1/\kappa}{v_g^0(k)}$ and then

$$200 \quad \frac{1}{2} A^R(\kappa) = \frac{1}{2} \tau^R(\kappa) E_\kappa(\kappa) = \frac{1}{2} \frac{1/\kappa}{v_g^0(k)} E_\kappa(\kappa), \quad (3.10)$$

201 where k denotes the wave wavenumber and κ the current wavenumber.

202 To calibrate an equivalent noise, we model \mathbf{v}' by $\sigma dB_t/dt$, where dB_t/dt is a spatio-
 203 temporal white noise and σ denotes a spatial filtering operator which encodes spatial
 204 correlations through its ADSD, $A_{\mathbf{v}'}^R$, and the horizontal incompressibility condition ($\nabla \cdot \sigma = 0$).
 205 For incompressibility, we work with the curl of a streamfunction. To generate a homogeneous
 206 and isotropic streamfunction, we can filter a one-dimensional white noise \check{B} with a filter $\check{\psi}_\sigma$
 207 (Resseguier *et al.* 2017b), that is $\check{\psi}_\sigma \star \check{B}$ where \star denotes a spatial convolution. The velocity
 208 field is hence :

$$209 \quad \mathbf{v}' = \sigma dB_t/dt = \nabla^\perp \check{\psi}_\sigma \star dB_t/dt, \quad (3.11)$$

210 with ∇^\perp the two-dimensional curl. That formula is easily written and implementable
 211 in Fourier space (see equation (A 2)). To define the streamfunction filter, we note that
 212 $\frac{\pi \kappa^3}{(2\pi)^2} |\widehat{\check{\psi}_\sigma}(\kappa)|^2 = \frac{1}{2} \oint_0^{2\pi} d\theta_\kappa \kappa \frac{\|\sigma dB_t(\kappa)\|^2}{(2\pi)^2 dt} = A_{\mathbf{v}'}^R(\kappa)$, i.e. the filter can be fully defined by the
 213 small-scale ADSD, $A_{\mathbf{v}'}^R$. To close our model, we assume an ADSD power law:

$$214 \quad A^R(\kappa) \approx A_0^R \kappa^{-\mu}. \quad (3.12)$$

215 It enables automatic closure calibration: $A_{\mathbf{v}'}^R(\kappa) = A_0^R \kappa^{-\mu} - A_{\mathbf{v}}^R(\kappa)$, from instantaneous
 216 large-scale current statistics $A_{\mathbf{v}}^R$ only (Resseguier *et al.* 2020b) as illustrated in figure 1.

217 4. Statistical wave dynamics

218 In a stochastic framework, the Stratonovich or Itô notations can both be used (Kunita
 219 1997; Oksendal 1998). Under Stratonovich calculus rules, expressions become similar
 220 to deterministic ones. Specifically, stochastic versions of linearized dynamical equations
 221 are obtained by replacing \mathbf{v} by $\bar{\mathbf{v}} + \sigma \circ dB_t/dt$. Then, the stochastic transport of phase,
 222 $\frac{d}{dt} \phi = \omega_0(\|\nabla \phi\|)$, i.e. – up to that velocity replacement – the Stratonovich dispersion
 223 relation is exactly (2.1). The method of characteristics also applies. Note, one can switch
 224 from Stratonovich to Itô notations, where \mathbf{v}' corresponds to $\sigma dB_t/dt$. The characteristics

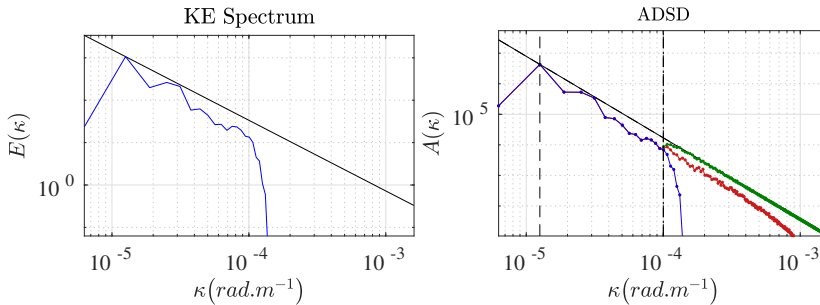


Figure 1: KE spectrum ($m^2 \cdot s^{-2} / (\text{rad} \cdot m^{-1})$) (left) and ADSD ($m^2 \cdot s^{-1} / (\text{rad} \cdot m^{-1})$) (right) of the resolved high-resolution velocity, A^R , in red, low-resolution velocity, $A_{\bar{v}}^R$, in blue, and modeled stochastic velocity, $A_{v'}^R(\kappa) = A_0^R \kappa^{-\mu} - A_{\bar{v}}^R(\kappa)$, in green. For the ADSD power law, $A^R(\kappa) \approx A_0^R \kappa^{-\mu}$, we impose the theoretical KE spectrum slope $-\frac{5}{3}$ (black solid line), coherently with homogeneous SQG dynamics (see "Numerical results" section). The residual ADSD (green line) is set to extrapolate that power law at small scales.

225 equations (2.2)-(2.3) also remain unchanged for homogeneous and isotropic v' :

$$226 \quad \begin{cases} d\mathbf{x}_r = (\mathbf{v}_g^0 + \bar{\mathbf{v}})dt + \sigma d\mathbf{B}_t, \\ d\mathbf{k} = -\nabla(\bar{\mathbf{v}}dt + \sigma d\mathbf{B}_t)^\top \mathbf{k}. \end{cases} \quad (4.1)$$

227 4.1. Single-ray stochastic differential equations

228 When studying a single ray in an homogeneous and isotropic turbulence (3.11), the wave-
229 vector dynamics simplifies. In the local crest-oriented frame, the influence of small scale
230 currents can be solely represented by four one-dimensional white noise forcings.

231 Notably, dynamics of wave-vectors (2.3) are similar to tracer gradient dynamics (Bühler
232 2009; Plougonven & Zhang 2014). Only the coupled ray path dynamics (2.2) differs.
233 Accordingly, we follow the notations and derivations of the mixing analysis from Lapeyre
234 *et al.* (1999) and references therein. Without loss of generality, the large-scale velocity can
235 be parameterized as

$$236 \quad \bar{\mathbf{v}} = \bar{v} \begin{pmatrix} \cos \bar{\theta} \\ \sin \bar{\theta} \end{pmatrix} \quad \text{and} \quad \nabla \bar{\mathbf{v}}^\top = \frac{1}{2} \begin{bmatrix} \bar{\sigma} \sin 2\bar{\phi} & \bar{\omega} + \bar{\sigma} \cos 2\bar{\phi} \\ -\bar{\omega} + \bar{\sigma} \cos 2\bar{\phi} & -\bar{\sigma} \sin 2\bar{\phi} \end{bmatrix}. \quad (4.2)$$

237 Figure 2 provides a synthetic view of angles involved. The dynamics wave group centroid \mathbf{x}_r
238 is directly driven by the large current wave group velocity, $\mathbf{v}_g^0 + \bar{\mathbf{v}}$. The influence of the large-scale
239 currents gradients on the wavevector dynamics (4.1), expressed in the local crest-oriented
240 frame ($\tilde{\mathbf{k}}, \tilde{\mathbf{k}}^\perp$), is straightforward (Lapeyre *et al.* 1999). The small-scale currents force the ray
241 dynamics through a stochastic noise. For a single ray $(\mathbf{x}_r, \mathbf{k}) = (x_r, y_r, k \cos \theta_k, k \sin \theta_k)$,
242 this noise can be rigorously described by four independent one-dimensional white noises
243 only (see Appendix A), $\dot{B}_t^{(1)}$, $\dot{B}_t^{(2)}$, $\dot{B}_t^{(3)}$, and $\dot{B}_t^{(4)}$, and:

$$244 \quad \frac{d}{dt} x_r = v_g^0 \cos \theta_k + \bar{v} \cos \bar{\theta} + \sqrt{a_0} \dot{B}_t^{(1)}, \quad (4.3)$$

$$245 \quad \frac{d}{dt} y_r = v_g^0 \sin \theta_k + \bar{v} \sin \bar{\theta} + \sqrt{a_0} \dot{B}_t^{(2)}, \quad (4.4)$$

$$246 \quad \frac{d}{dt} \log k = -\bar{\sigma} \sin(\zeta) + \gamma_0 + \sqrt{\gamma_0} \dot{B}_t^{(3)}, \quad (4.5)$$

$$247 \quad \frac{d}{dt} \theta_k = \frac{1}{2}(\bar{\omega} - \bar{\sigma} \cos(\zeta)) + \sqrt{3\gamma_0} \dot{B}_t^{(4)}, \quad (4.6)$$

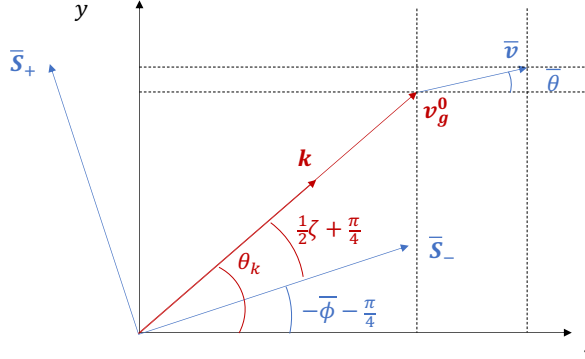


Figure 2: Schematic view of vectors and angles involved in single-ray dynamics. \bar{S}_- and \bar{S}_+ are respectively compression and dilatation axes associated with the large-scale velocity gradient $\nabla \bar{\mathbf{v}}^\top$.

248 where $\zeta = 2(\theta_k + \bar{\phi})$ and

$$249 \quad a_0 = \frac{1}{2dt} \mathbb{E} \|\sigma dB_t\|^2 = \int_0^{+\infty} A_{v'}^R(\kappa) d\kappa, \quad (4.7)$$

$$250 \quad \gamma_0 = \frac{1}{8dt} \mathbb{E} \|\nabla_x(\sigma dB_t)^\top\|^2 = \frac{1}{4} \int_0^{+\infty} k^2 A_{v'}^R(\kappa) d\kappa. \quad (4.8)$$

251 Diffusivity constants depend through (3.10) on both the correlation length and the spectrum
 252 slope of the small-scale velocity. In contrast to the classical fast wave approximation, the
 253 wavenumber does vary. This is due to (i) the finite large-scale strain rate, $\bar{\sigma}$, and (ii) the
 254 small-scale isotropic velocity model (3.11). This isotropy assumption and its implication are
 255 discussed in Appendix C. Note that neither large-scale nor small-scale component is assumed
 256 to be steady, even though that Eulerian velocity unsteadiness is only a secondary process in
 257 the wave dynamics. The fast temporal variations seen by the wave are mainly driven by the
 258 large wave speed and not by the Eulerian velocity unsteadiness. The current unsteadiness can
 259 also lead to wavenumber variations (Dong *et al.* 2020; Cox *et al.* 2023; Boury *et al.* 2023).
 260 Given a known wavevector angle, it leads to a wavenumber evolution

$$261 \quad k(t) = k(0) \exp\left(-\int_0^t \bar{\sigma} \sin(2(\theta_k + \bar{\phi})) dt'\right) \exp\left(\gamma_0 t + \sqrt{\gamma_0} B_t^{(3)}\right), \quad (4.9)$$

262 and hence to the complete wavevector distribution, i.e. the wave spectrum. The second
 263 exponential factor in (4.9) is a geometric Brownian motion. Its mean diverges in time
 264 exponentially rapidly. Physically, shear and strain of \mathbf{v}' tends to shorten the wavelength
 265 ((Voronovich 1991; Boury *et al.* 2023)) leading to this exponential divergence. This factor
 266 has a log-normal distribution, suggesting possible extreme transient wavenumber events.
 267 This generalizes previous results Voronovich (1991); Klyatskin & Koshel (2015), obtained
 268 with neglecting the time-correlated current component, $\bar{\mathbf{v}}$.

269 For completeness, the action distribution over space and wave vector can be derived. Some
 270 approaches consider finite-size wave trains either through additional equations (Jonsson
 271 1990; White & Fornberg 1998) or re-meshing (Hell *et al.* in preparation). Otherwise,
 272 each ray transports its action spectrum (2.6) and we need to numerically combine many
 273 rays (Lavrenov 2013), or rely on analytic approximations. Typically, we solve (4.3)-(4.5)
 274 exhibiting, $p(\mathbf{x}, \mathbf{k} | \mathbf{x}_r^0, \mathbf{k}_r^0, t)$, the distribution of the ray (\mathbf{x}, \mathbf{k}) at time t given initial conditions

275 $(\mathbf{x}_r^0, \mathbf{k}^0)$. Then, by analogy with tracers in incompressible turbulence (Piterbarg & Ostrovskii
 276 1997, equation (1.31), see also Appendix D) we can evaluate the wave action spectrum mean
 277 – or any point-wise statistics – as follows

$$278 \quad \mathbb{E}N(\mathbf{x}, \mathbf{k}, t) = \iint d\mathbf{x}_r^0 d\mathbf{k}^0 N^0(\mathbf{x}_r^0, \mathbf{k}_r^0) p(\mathbf{x}, \mathbf{k} | \mathbf{x}_r^0, \mathbf{k}^0, t), \quad (4.10)$$

279 where N^0 is the initial wave action spectrum. Integrating this expression over wavevectors,
 280 we note that the distribution inside the integrals changes

$$281 \quad \mathbb{E}A(\mathbf{x}, t) = \iint d\mathbf{x}_r^0 d\mathbf{k}^0 N^0(\mathbf{x}_r^0, \mathbf{k}_r^0) p(\mathbf{x} | \mathbf{x}_r^0, \mathbf{k}^0, t). \quad (4.11)$$

282 The wave action mean solely depends of group positions distribution. Multi-point action
 283 statistics – e.g. focusing $\mathbb{E}\|\nabla_x A\|^2$ – rely on multi-ray correlations, encoded in the stochastic
 284 characteristic equations (4.1), but not the simplified model (4.3)-(4.6). Alternatively, Eulerian
 285 descriptions of wave action dynamics directly provide action distribution over space and wave
 286 vector.

287 4.2. Eulerian dynamics and action diffusion

288 Wave action spectrum is transported along a 4-dimensional volume-preserving stochastic
 289 flow (4.1). Again by analogy with incompressible turbulence (Resseguier *et al.* 2017a), the
 290 stochastic transport of wave action spectrum in Itô notations reads

$$291 \quad \partial_t N + (\mathbf{v}_g^0 + \bar{\mathbf{v}} + \sigma \frac{d\mathbf{B}_t}{dt}) \cdot \nabla_x N + \left(-\nabla_x (\bar{\mathbf{v}} + \sigma \frac{d\mathbf{B}_t}{dt})^\top \mathbf{k} \right) \cdot \nabla_k N \\
 292 \quad = \begin{bmatrix} \nabla_x \\ \nabla_k \end{bmatrix} \cdot \left(\mathbf{D} \begin{bmatrix} \nabla_x \\ \nabla_k \end{bmatrix} N \right) = \frac{1}{2} a_0 \Delta_x N + \frac{1}{2} \gamma_0 \frac{1}{k} \partial_k \left(k^3 \partial_k N \right) + \frac{3}{2} \gamma_0 \partial_{\theta_k}^2 N. \quad (4.12)$$

293 The RHS is reminiscent to Eq. (3.16) in Bôas & Young (2020) and Eq. (36) in Smit &
 294 Janssen (2019), and more generally to rapid wave models. Nevertheless, equation (4.12) is
 295 not averaged and explicitly involves large-scale currents and noise terms (terms with factor
 296 $\frac{d\mathbf{B}_t}{dt}$). Differences with Smit & Janssen (2019); Bôas & Young (2020) for the diffusivity
 297 estimates and the detailed computation of the 4×4 diffusion matrix \mathbf{D} can be found in
 298 Appendix A. Itô notations of (4.12) explicitly separate mean terms (e.g. diffusion terms) and
 299 zero-mean noise terms. Here, the Eulerian Itô notations reveal that coefficients $\frac{1}{2}a_0$, $\frac{1}{2}\gamma_0$, and
 300 $\frac{3}{2}\gamma_0$ act to diffuse wave action in space, wavenumber and wave-vector angle, respectively.

301 5. Numerical experiments

302 To illustrate these developments, we consider ocean surface gravity waves propagating over
 303 a dynamical flow region. Ray tracing through synthetic surface currents will provide a
 304 benchmark. It will be shown that a broad range of the current scales can be replaced by
 305 the stochastic parametrization (3.11) without affecting ray scattering and action distribution.
 306 Theoretical results (4.3)-(4.12) will suggest approximate analytic solutions.

307 5.1. Surface current dynamics

308 Simplified upper ocean dynamics are considered to follow:

$$309 \quad (\partial_t + \mathbf{v} \cdot \nabla) \Theta = 0 \quad \text{with} \quad \mathbf{v} = -\nabla^\perp (-\Delta)^{-\xi} \Theta, \quad (5.1)$$

310 where Θ stands for the buoyancy, ∇^\perp the curl and Δ the Laplacian. Two extreme cases: the
 311 Surface Quasi-Geostrophic dynamics ($\xi = \frac{1}{2}$) (Held *et al.* 1995; Lapeyre 2017), abbreviated

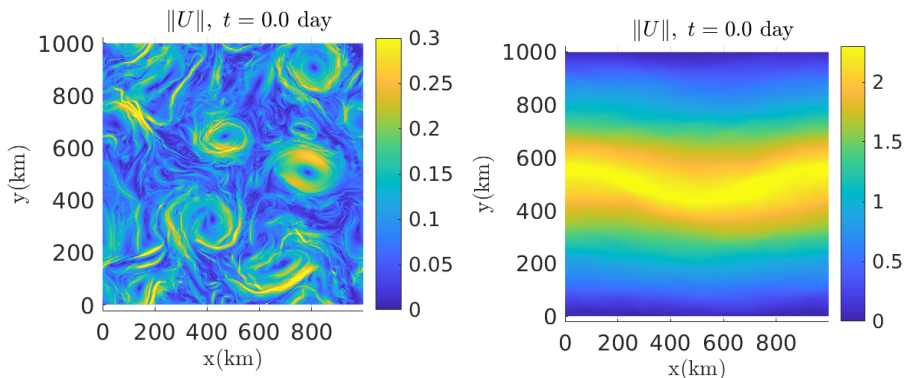


Figure 3: Current velocity norm of the SQG homogeneous turbulence (left) and of the 2D Euler jet current at high-resolution (512×512).

312 SQG, and the two-dimensional Euler dynamics ($\xi = 1$), abbreviated 2D Euler. SQG is
 313 dynamics with an extreme locality (KE spectrum slope $-5/3$) whereas 2D Euler has an
 314 extreme non-locality (KE spectrum slope -3). The objective is to test how the proposed
 315 closures apply to both dynamics to be equally useful for any more realistic upper ocean
 316 dynamics. Additionally, test cases are developed to assess the multiscale stochastic closure
 317 in both homogeneous and heterogeneous propagating medium. Moreover, we would like to
 318 challenge our closure beyond the validity of rapid wave models. In our first test case, surface
 319 fast waves travel in a homogeneous and isotropic SQG turbulence. Then, we simulate waves
 320 propagating in a spatially heterogeneous 2D Euler turbulence, mimicking an oceanic jet. For
 321 both SQG and 2D Euler dynamics, a reference simulation is obtained at a resolution 512×512
 322 for a 1000-km squared domain, with the help of a pseudo-spectral code (Resseguier *et al.*
 323 2017b, 2020b). Once initialized, the current velocity \mathbf{v} is about $0.1 \text{ m}\cdot\text{s}^{-1}$ for the homogeneous
 324 turbulence and $1 \text{ m}\cdot\text{s}^{-1}$ for the jet (see figure 3).

325

5.2. Rays scattering in homogeneous SQG turbulence

326 A wave system enters the bottom boundary, propagating to the top. The carrier incident wave
 327 has an intrinsic wave group velocity of 10 m/s , i.e. wavelength $\lambda = 250 \text{ m}$. Its envelope
 328 is Gaussian with an isotropic spatial extension of 30λ . The left panels of figures 4 and
 329 5 illustrates the resulting dynamics, spreading the wavevectors (figure 5) of the incoming
 330 waves. From bottom to top, spectral diffusion occurs (figure 5), in the direction orthogonal
 331 (here k_x) to the propagation (here k_y), in line with the additive noise appearing in equation
 332 (4.6). This scattering accelerates – along the propagation – the wave position spread (figure
 333 4). This acceleration is explained by the ray equation (4.3) dominated by the intrinsic wave
 334 group velocity.

335 To mimic a badly resolved $\bar{\mathbf{v}}$ field, \mathbf{v} is smoothed at a resolution 32×32 . Using this
 336 coarse-scale current, middle panels of figures 4 and 5, the scattering – described in the
 337 previous paragraph – is strongly depleting in comparison to ray tracing in fully-resolved
 338 turbulence. The spectral diffusion induced by small-scale turbulence is missing. Thus, the
 339 spatial spreading also is narrower compared to high-resolution simulations. A stochastic
 340 current \mathbf{v}' is then added for ray tracing (4.1). This stochastic component is divergence-free
 341 and has a self-similar distribution of energy across spatial scales (3.11) (see figure 1). The
 342 resulting spatial and spectral spreads are now comparable to simulations with high-resolution

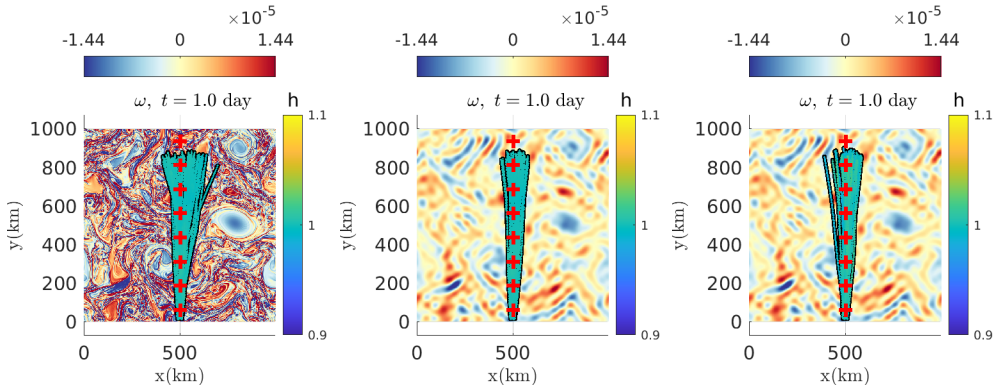


Figure 4: Swell (wavelength $\lambda = 250$ m) interacting with a high-resolution (512×512) deterministic SQG current (left), a low-resolution (32×32) deterministic SQG current (middle) and a low-resolution (32×32) deterministic SQG current plus (one realization of) the time-uncorrelated stochastic model (right) – colored by the corresponding wave amplitude, $h(t) = \sqrt{\omega_0(k(t))N(t=0)}$ (right-hand side colorbar) – computed by forward advection and superimposed on the current vorticity $\omega = \nabla^\perp \cdot \mathbf{v}$. The red cross indicate where the bidirectional wave spectra of figure 5 are computed.

343 currents. For this setting, the stochastic closure provides satisfying results for a sufficiently
 344 well-resolved large-scale current. The key decorrelation ratio $\epsilon = \frac{l_v'}{l_v} \frac{\|\mathbf{v}\|}{v_g^0}$ indeed depends on
 345 the resolution through l_v' . The large-scale current $\bar{\mathbf{v}}$ is resolved on a 32×32 grid, i.e. with a
 346 resolution $l_v' = \frac{\|\nabla \mathbf{v}^T\|}{\|\nabla \mathbf{v}^T\|} l_v = 0.33 l_v$. As such $\epsilon = 4.1 \times 10^{-3}$, computed with $v_g^0 \approx 10$ m.s $^{-1}$
 347 and $\|\mathbf{v}\| \approx 0.12$ m.s $^{-1}$, so $\frac{\|\mathbf{v}\|}{v_g^0} \approx 1.2 \times 10^{-2}$, which is sufficiently small to make the proposed
 348 model applicable.

349 From the ADSD estimate (equation (3.10) illustrated by figure 1) and (4.7)-(4.8), eval-
 350 uations of the diffusivity coefficients a_0 and γ_0 are straightforward. Previously discussed
 351 Smit & Janssen (2019), the spatial diffusivity is extremely weak: $a_0 = 6.4 \times 10^{-1}$ m 2 .s $^{-1}$
 352 (spatial variations in ray equations (4.3)-(4.4) of about $\sqrt{a_0 t} = 230$ m during 1 day). In
 353 contrast, the spectral angle diffusivity is large: $3\gamma_0 = 3.0 \times 10^{-8}$ rad 2 .s $^{-1}$. Along our 1-day
 354 simulation, neglecting large-scale velocity influence, (4.6) leads to a Brownian wave vector
 355 angle variations $\delta\theta_k = \theta_k - \theta_k(0) = \sqrt{3\gamma_0} B_t^{(4)}$ with a standard deviation $\sigma_{\delta\theta_k} = \sqrt{3\gamma_0 t} =$
 356 5.2×10^{-2} rad $\approx 3.0^\circ$, eventually increasing the wave group spectral maximal extension from
 357 $\pm 2\sigma_{k_x} = \pm 2 \frac{2\pi}{30\lambda} = \pm 1.7 \times 10^{-3}$ rad.m $^{-1}$ to $\pm 2\sigma_{k_x} \approx \pm 2 \sqrt{\left(\frac{2\pi}{30\lambda}\right)^2 + (k\sigma_{\delta\theta_k})^2} = \pm 3.1 \times 10^{-3}$
 358 rad.m $^{-1}$, confirmed by figure 5. This figure also illustrates the wave action diffusion induced
 359 by diffusivity γ_0 , well predicted by the Eulerian wave action model (4.12). In this scattering
 360 regime, the increased angle variability leads, by advection, to a spatial spread. The simplified
 361 ray equation (4.3) gives $\delta x \approx \int_0^t v_g^0 \cos \theta_k dt' \approx v_g^0 \int_0^t \delta\theta_k dt' \approx v_g^0 \sqrt{3\gamma_0} \int_0^t B_{t'}^{(4)} dt'$ with
 362 maximal extension $\pm 2\sigma_x \approx \pm 2v_g^0 \sqrt{\gamma_0 t^3} \approx \pm 52$ km, in agreement with figure 4. Finally, we
 363 estimate a first-order delay along the propagation $\delta t = t - (y - y(0))/v_g^0 \approx \int_0^t (1 - \sin \theta_k) dt' \approx$
 364 $\frac{1}{2} \int_0^t \delta\theta_k^2 dt' \approx \frac{3}{2} \gamma_0 \int_0^t (B_{t'}^{(4)})^2 dt'$, with mean value $\mathbb{E}\delta t = \frac{3}{4} \gamma_0 t^2$.

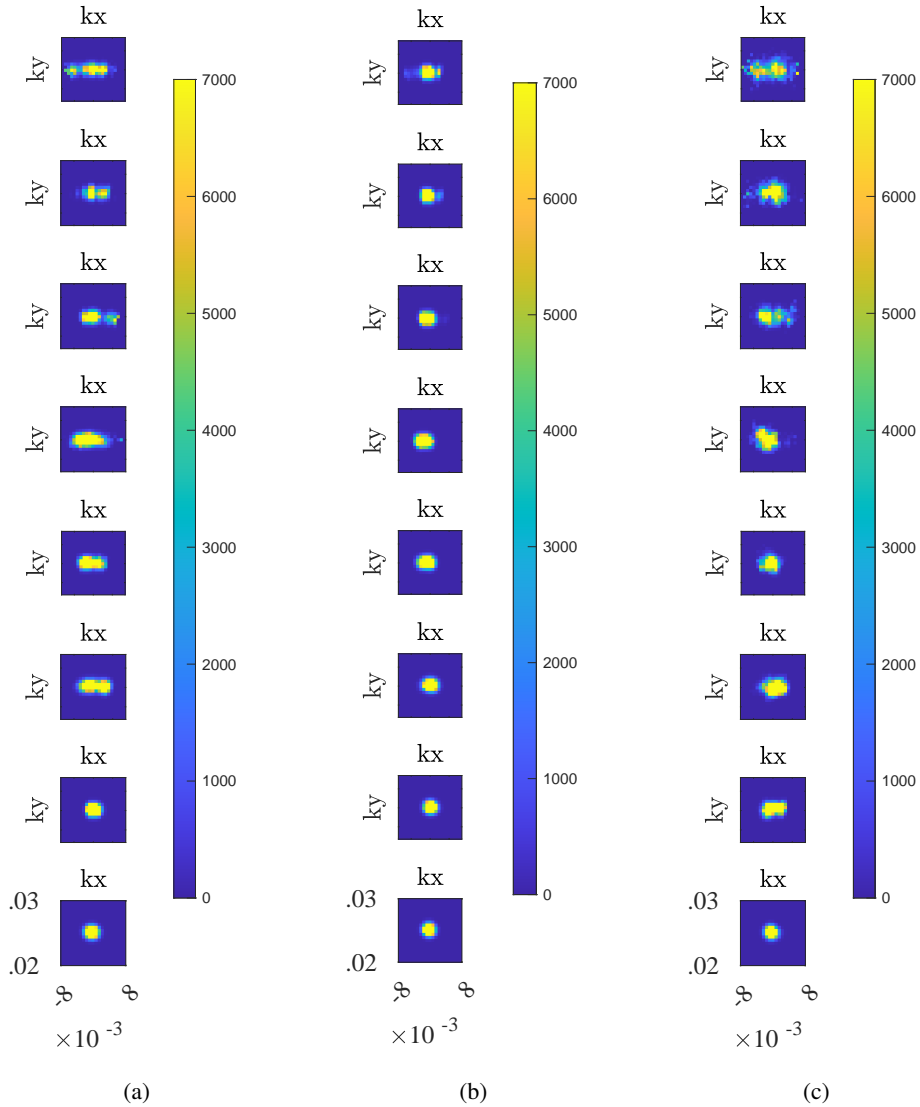


Figure 5: Bidirectional wave spectra, computed by backward advection, at 8 locations along a vertical axis (the mean wave propagation direction) resulting from a swell interacting with a high-resolution (512×512) deterministic SQG current (panel (a)), a low-resolution (32×32) deterministic SQG current (panel (b)) and a low-resolution (32×32) deterministic SQG current plus (one realization of) the stochastic model (3.11) (panel (c)). The spatial locations where the spectra are calculated are highlighted on figure 4 by the red crosses.

365

5.3. Wave groups trapped in a 2D Euler turbulent jet

366 Tests are now performed for rays traveling in fast and strongly heterogeneous 2D Euler flows.
 367 Classical fast wave models – assuming flows of weak amplitude and often uniform statistics –
 368 are expected to fail here. Jets exhibit strong current gradients (e.g. Kudryavtsev *et al.* 2017)
 369 creating strong ray focusing and possibly rogue events. Passing through localized spatial
 370 structures, caustics can appear but solely from unrealistically collimated wave trains (White
 371 & Fornberg 1998; Heller *et al.* 2008; Wang *et al.* 2023). Occurrences strongly reduce for

372 finite directional spread (Slunyaev & Shrira 2023). Here, wave groups are trapped in a jet, but
 373 nonlinear wave interactions are neglected. The high-resolution numerical simulations (see
 374 figure 6) reveal that even linear wave trains are well trapped in adversarial currents. Freund
 375 & Fleischman (2002) observed a similar behavior for acoustic waves in a 3D turbulent jet.
 376 Note that during our simulation, rays cross the domain several times (because of the doubly
 377 periodic boundary conditions, see Appendix E for technical details). Top (resp. bottom) of
 378 the jet, the vorticity and thus – at first order – rays curvatures (Dysthe 2001) are negative
 379 (resp. positive). Therefore, rays oscillate around the jet. A toy model can explain this behavior.
 380 Following the multiscale stochastic approach (4.3)-(4.6), wave scattering is also taken into
 381 account.

382 For very-coarsened-grained (4×4) current \bar{v} , oscillation remains, but most of the scattering
 383 vanishes, as illustrated by figure 7. Moreover, the curvature of the jet creates artificial wave
 384 focusing at $t = 8$ and 10 days. Introducing a time-uncorrelated model (3.11) corrects the
 385 resolution issue on figure 8. Figure 9 plots the current ADSD. The current is strong ($\|\mathbf{v}\| \approx 1.4$
 386 m.s^{-1}), and the usual fast wave approximation cannot be applied ($\frac{\|\mathbf{v}\|}{v_g^0} \approx 1.2 \times 10^{-1}$). However,
 387 the proposed modified fast wave model is valid, even at the very coarse 4×4 resolution.
 388 Indeed, 2D Euler spectra are steeper than for SQG dynamics, and the length scale ratio is
 389 already significant at this resolution, $\frac{l_v'}{l_v} = 0.14$, and the derived time-decorrelation ratio is
 390 small: $\epsilon = \frac{l_v'}{l_v} \frac{\|\mathbf{v}\|}{v_g^0} = 1.6 \times 10^{-2}$.

391 Furthermore, by approximating the under-resolved current \bar{v} , an analytic stochastic solution
 392 can be obtained for a ray traveling against the current. The large-scale pattern of the jet takes
 393 a quadratic form

$$394 \quad \bar{u} \approx \bar{U}_0 - \frac{1}{2}\bar{\beta} \left(y - \frac{L_y}{2} \right)^2 \quad \text{and} \quad \bar{v} \approx 0, \quad \text{with} \quad \bar{U}_0, \bar{\beta} < 0. \quad (5.2)$$

395 Note, the toy model (5.2) simply considers a straight jet, neglecting its curvature. For weak
 396 subgrid currents and a ray, $(x_r, y_r' + \frac{L_y}{2}, k, \theta_k)$, propagating mainly to the right, θ_k is small
 397 and the simplified ray equation (4.4) determines the group position with respect to the jet y_r'

$$398 \quad \frac{d}{dt} y_r' \approx v_g^0 \sin(\theta_k) = v_g^0 \theta_k + O(\theta_k^2). \quad (5.3)$$

399 For frozen turbulence, the wave-number and hence v_g^0 will not significantly vary. The other
 400 ray equation (4.3) localizes the group along the jet, $x_r \approx x_r(0) + (v_g^0 - \bar{u})t$, dropping the
 401 $O(\theta_k^2)$ from now on. Moreover, $\tilde{\mathbf{k}}^\perp \cdot \nabla \bar{v}^\top \tilde{\mathbf{k}} \approx -\partial_y \bar{u}$ and the dynamics of wave vector angle
 402 (4.6) simplifies to a stochastic oscillator equation:

$$403 \quad \frac{d^2}{dt^2} y_r' = v_g^0 \frac{d}{dt} \theta_k = -\partial_y (v_g^0 \bar{u}) + v_g^0 \sqrt{3\gamma_0} \dot{B}_t^{(4)} = -\bar{\omega}_r^2 y_r' + v_g^0 \sqrt{3\gamma_0} \dot{B}_t^{(4)}. \quad (5.4)$$

404 with $\bar{\omega}_r = \sqrt{|v_g^0 \bar{\beta}|}$. Here $v_g^0 \bar{u}$ plays the role of a potential, trapping the rays in the jet vicinity,
 405 whereas the noise accounts for wave scattering. Solution of this linear equation is known
 406 (e.g. Resseguier *et al.* 2017a, Eq.(51)-(55)):

$$407 \quad y_r(t) = \underbrace{\frac{L_y}{2} + y_r'(0) \cos(\bar{\omega}_r t) + \frac{v_g^0}{\bar{\omega}_r} \theta_k(0) \sin(\bar{\omega}_r t)}_{=\mathbb{E}(y_r(t))} + \underbrace{Y_{\gamma_0} \sqrt{\bar{\omega}_r} \int_0^t \sin(\bar{\omega}_r(t-r)) dB_r^{(4)}}_{=y_r''(t)}, \quad (5.5)$$

408 with $Y_{\gamma_0} = v_g^0 \sqrt{3\gamma_0/\bar{\omega}_r^3}$. The wavevector angle solution is similar. The solution ensemble

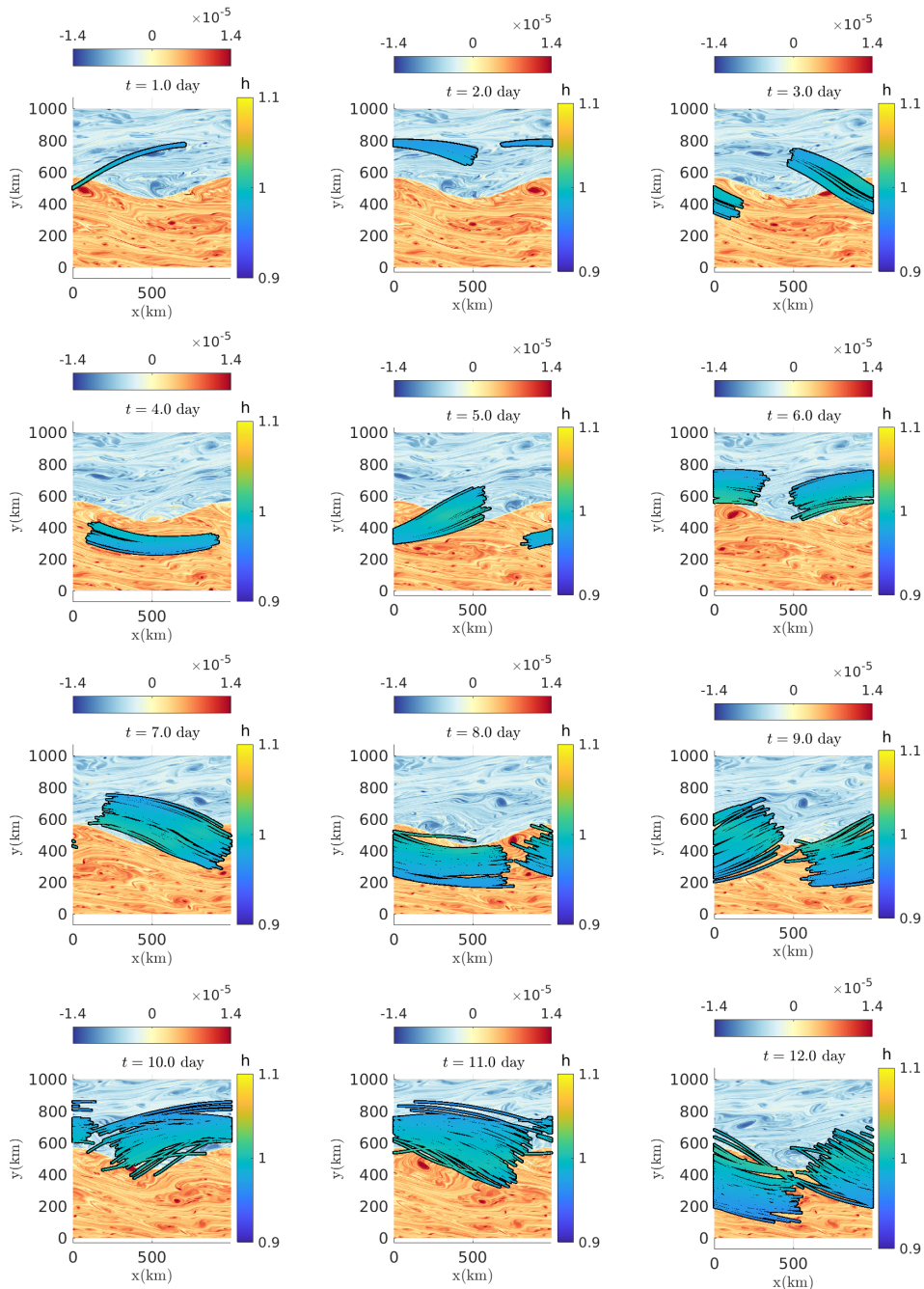


Figure 6: Rays facing a high-resolution (512×512) deterministic 2D Euler jet current – colored by the corresponding wave amplitude, $h(t) = \sqrt{\omega_0(k(t))}N(t=0)$ (right-hand side colorbar) – computed by forward advection and superimposed on the current vorticity $\omega = \nabla^\perp \cdot \mathbf{v}$ (top colorbar).

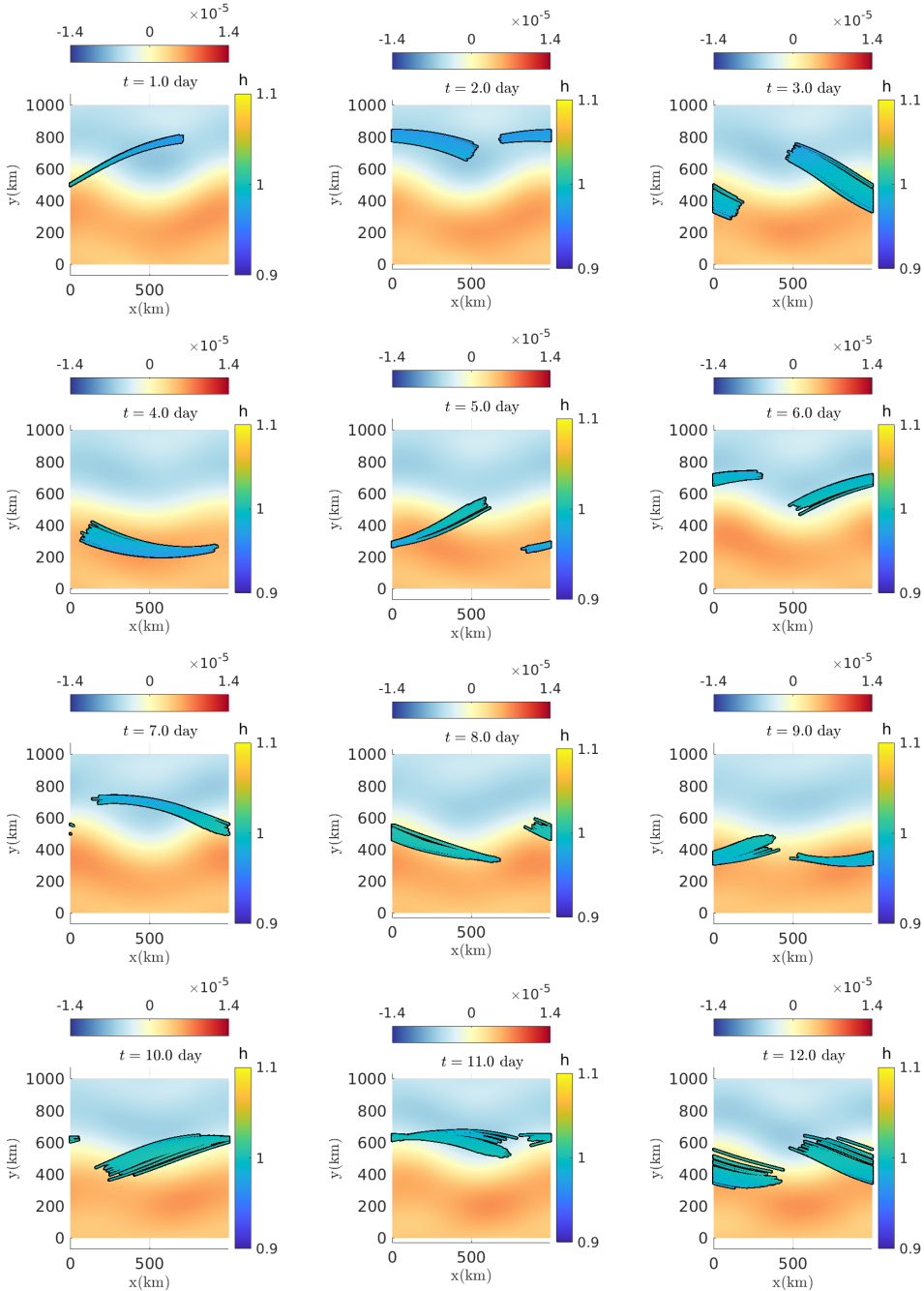


Figure 7: Rays facing a low-resolution (4×4) deterministic 2D Euler jet current – colored by the corresponding wave amplitude, $h(t) = \sqrt{\omega_0(k(t))}N(t=0)$ (right-hand side colorbar) – computed by forward advection and superimposed on the current vorticity $\omega = \nabla^\perp \cdot \mathbf{v}$ (top colorbar).

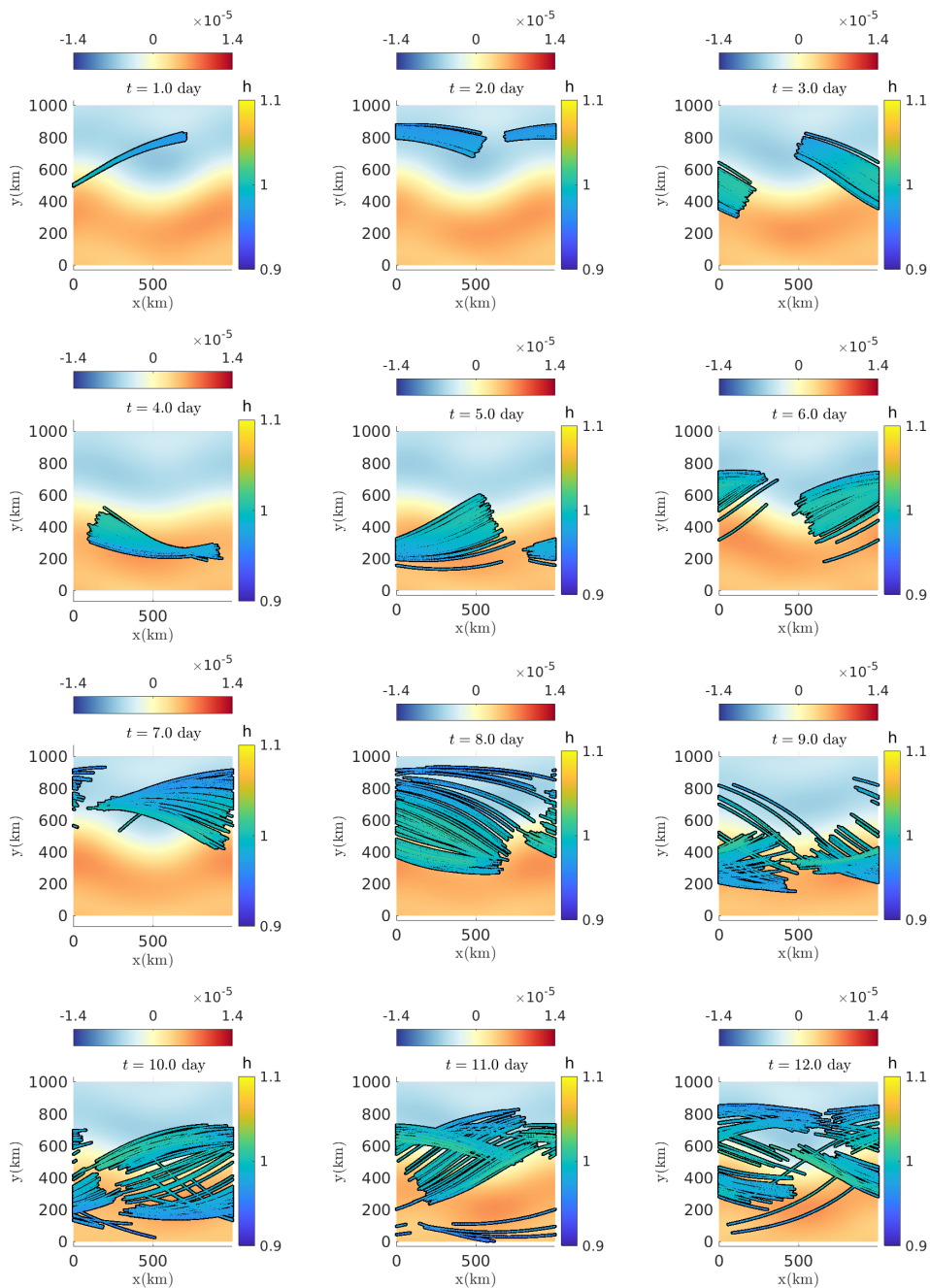


Figure 8: Rays facing a low-resolution (4×4) deterministic 2D Euler jet current plus (one realization of) the time-uncorrelated stochastic model – colored by the corresponding wave amplitude, $h(t) = \sqrt{\omega_0(k(t))}N(t=0)$ (right-hand side colorbar) – computed by forward advection and superimposed on the low-resolution current vorticity $\bar{\omega} = \nabla^\perp \cdot \bar{\mathbf{v}}$ (top colorbar).

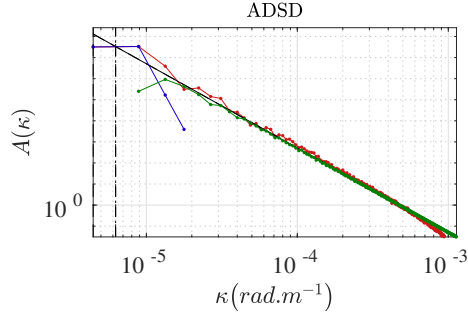


Figure 9: ADSD ($m^2 \cdot s^{-1} / (\text{rad} \cdot m^{-1})$) of the resolved high-resolution jet velocity in red, low-resolution jet velocity in blue, and modeled stochastic velocity, in green. The theoretical spectrum slope -3 (black solid line) is imposed, consistent with homogeneous 2D Euler dynamics. The residual ADSD (green line) is set to extrapolate that power law at small scales.

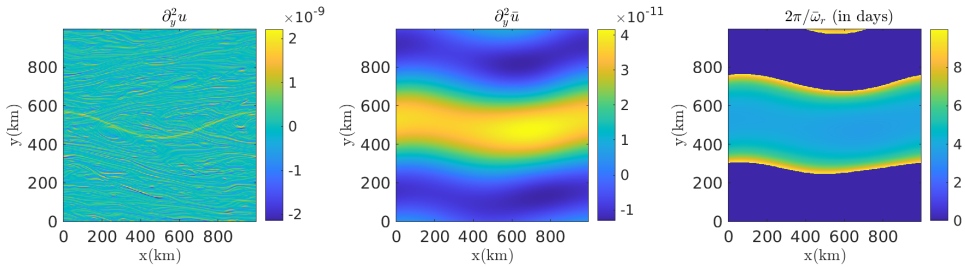


Figure 10: Vorticity shear $\partial_y^2 u$ of the deterministic 2D Euler jet current at high-resolution (512×512) (left), at low-resolution (4×4) (middle), and the corresponding swell system period $2\pi/\bar{\omega}_r$. Far from the jet (± 200 km away), the vorticity shear becomes zero or even positive, so period larger than 10 days are cropped.

409 mean, $\mathbb{E}y_r$, is a simple coherent deterministic oscillator. This mean solution describes well
 410 the interaction between the group and the under-resolved current from figure 7. From the
 411 coarse-scale vorticity shear plotted in figure 10 in the vicinity of the jet, we can estimate
 412 $\bar{\beta} = -2.7 \times 10^{-11} \text{m}^{-1} \cdot \text{s}^{-1}$. It yields an oscillation frequency $\bar{\omega}_r = 1.3 \times 10^{-5} \text{rad} \cdot \text{s}^{-1}$ i.e. a
 413 period of $2\pi/\bar{\omega}_r = 5.7$ days, in agreement with the ray tracing simulations. Note that the
 414 high-resolution vorticity shear, left panel of figure 10, does not suggest any relevant values
 415 to explain the ray oscillations. Only the proposed multiscale current decomposition provides
 416 a quantitative explanation for these oscillations, and by extension for trapping rays inside the
 417 jet. Added to the mean solution, the random parts, $y_r''(t)$, are continuous summations of zero-
 418 mean incoherent wave fluctuations. At each time r , the additive random forcing introduces
 419 an oscillation. But, the influence of the past excitations is weighed by sine wave due to the
 420 phase change. The group position and wavevector angle are Gaussian random variables (as
 421 linear combinations of independent Gaussian variables). Therefore, their finite dimensional
 422 law (i.e. the multi-time probability density function) are entirely defined by their mean and
 423 covariance functions. Specifically,

$$424 \mathbb{E} (y_r''(t) y_r''(t + \tau)) = \frac{1}{4} Y_{\gamma_0}^2 (\cos(\bar{\omega}_r \tau) (2\bar{\omega}_r t - \sin(2\bar{\omega}_r t)) + \sin(\bar{\omega}_r \tau) (1 - \cos(2\bar{\omega}_r t))). \quad (5.6)$$

425 In particular, the variance of the vertical positions reads $\sigma_y^2(t) = \frac{1}{4} Y_{\gamma_0}^2 (2\bar{\omega}_r t - \sin(2\bar{\omega}_r t))$. At

426 $t = 2\pi/\bar{\omega}_r$, the group has oscillated once around the jet and the maximal position extension
 427 reaches $\pm 2\sigma_y = \pm 2\sqrt{\pi} Y_{\gamma_0} = \pm 42$ km, well confirmed by ray simulations. In contrast, usual
 428 fast wave models (e.g. Smit & Janssen 2019) do not consider the interplay between smooth
 429 and rough currents, and hence solely predict a classical scattering with a much faster vertical
 430 location spreading: $\pm 2\sigma_y = \pm 2\sqrt{(2\pi)^3/3} Y_{\gamma_0} = \pm 217$ km. For large time, our multiscale
 431 approach predicts a scaling in t , much slower than the usual scattering t^3 scaling.

432 From the group vertical location and wavevector angle, we can also solve (4.5) an-
 433 alytically to estimate the group wavenumber variations. For small wavevector angles,
 434 $-\int_0^t \bar{\sigma} \sin(\zeta) dt' \approx 2 \int_0^t \bar{\omega} \theta_k dt' = 2\bar{\beta} \int_0^t y'_r \theta_k dt'$ and (4.9) together with the analytic
 435 solutions for y'_r and θ_k give a closed stochastic expression for the group wavenumber. Thus,
 436 the wavenumber factor $\exp(2\bar{\beta} \int_0^t y'_r \theta_k dt')$ oscillates at frequency $2\bar{\omega}_r$ and the oscillations
 437 modulate the wave amplitude: $h = \sqrt{E} = \sqrt{\omega_0 N} = \text{cst.} k^{\frac{1}{4}}$. The modulations are associated
 438 with wave-current energy exchanges Boury *et al.* (2023), visible in the colored rays, figures
 439 6, 7 and 8, when the groups enter and exit the jet.

440 Finally, the conditional ray distribution, $p(x, \mathbf{k} | \mathbf{x}_r^0, \mathbf{k}^0, t)$, the action spectrum mean from
 441 (4.10) and the action mean from (4.11) can all be derived. For a system initially localized
 442 in $(0, \frac{L_y}{2})$ with action A^0 , wavenumber k^0 and a $\sigma_{\delta\theta_k}^0$ -width Gaussian angular spreading,
 443 propagating to the right, the action mean reads

$$444 \quad \mathbb{E}A(x, y, t) = A^0 \delta \left(x - (v_g^0(k^0) - \bar{u}(y))t \right) \mathcal{N} \left(y - \frac{L_y}{2} \middle| \tilde{\sigma}_y^2(t) \right), \quad (5.7)$$

445 with $\mathcal{N} \left(\bullet \middle| \tilde{\sigma}_y^2(t) \right)$, a Gaussian function with variance $\tilde{\sigma}_y^2(t) = \sigma_y^2(t) + \left(\frac{v_g^0}{\bar{\omega}_r} \sin(\bar{\omega}_r t) \sigma_{\delta\theta_k}^0 \right)^2$.
 446 The action is advected in the horizontal direction, and slowly diffuses along the vertical
 447 direction.

448 6. Conclusion

449 Developed to generalize the ray-path concept for waves propagating over an heterogeneous
 450 turbulence, a practical stochastic framework is derived. For fast waves, the smallest scales
 451 of a turbulent flow decorrelate along the wave propagation. Flows with steeper spectra
 452 decorrelate faster, leading to a broader validity range of fast wave approximations. The
 453 proposed framework encodes both large-scale refraction and random scattering effects on
 454 wave statistical properties. The mean wave-action statistics are directly linked to resolved
 455 strain-rate and vorticity, but also to unresolved KE spectral properties. Both Eulerian and
 456 Lagrangian views are presented. A convenient calibration method is also proposed for the
 457 subgrid parametrization.

458 As anticipated, random horizontal currents delay wave arrival and augment the initial
 459 radiative transport equation with a directional diffusive term. These phenomena are illustrated
 460 with numerical simulations, analytical solutions, and quantitative proxies describing weak
 461 homogeneous turbulence. Using these proxies, measured delays in ray arrivals, estimated
 462 wave energy spectral characteristics and decays, and/or varying directional spread shall then
 463 be used to more quantitatively interpreted the upper the turbulent underlying flow properties.

464 The generalized fast wave approximation does takes into account wavenumber variation
 465 and handles strong heterogeneous flows, like localized jets with strong current gradients. As
 466 compared to numerical simulations, numerical and theoretical results explain and quantify
 467 ray trapping effects by jets, unlike usual fast wave approaches.

468 Among fast wave literature, isotropic diffusion and, hence, wavenumber diffusion may (e.g.
 469 Voronovich 1991) or may not (e.g. Bôas & Young 2020) comes into play (see Appendix

470 **C** for details). Future works could adapt our convenient stochastic calculus framework to
 471 the second models family. Besides, further analytical developments could consider finite-
 472 size wave groups, their dynamics (Jonsson 1990; White & Fornberg 1998) and statistical
 473 distributions, or alternatively the Eulerian action dynamics (4.12) with all its multi-point
 474 stochastic structure. When achieved, this next theoretical development could provide new
 475 means to analyze wave dynamics with subsequent fast simulations of ensembles. Beside
 476 comprehension and analysis, our stochastic simulation tools aim at eventually facilitate
 477 future ensemble-based data assimilation algorithms (Smit *et al.* 2021).

478 **Funding.** This work is supported by the R&T CNES R-S19/OT-0003-084, the ERC project 856408-STUOD,
 479 the European Space Agency World Ocean Current project (ESA Contract No. 4000130730/20/I-NB), and
 480 SCALIAN DS.

481 **Declaration of interests.** The authors report no conflict of interest.

482 **Data availability statement.** SCALIAN DS owns a portion of the developed code intellectual property.
 483 For commercial reasons, that code will remain private.

484 **Author ORCIDs.** V. Resseguier, <https://orcid.org/0000-0002-9301-9493>; E. Hascoët <https://orcid.org/0009-0002-0760-6534>; B. Chapron, <https://orcid.org/0000-0001-6088-8775>

486 **Author contributions.** VR developed the theory. VR and EH wrote the code and performed numerical
 487 experiments. VR and BC wrote the paper.

488 Appendix A. Stochastic forcing covariance

489 In this appendix, we will compute the conditionnal covariance of the stochastic forcing of
 490 our eikonal characteristic equations (4.1), that is:

$$491 \quad 2\mathbf{D} \triangleq \frac{1}{dt} \mathbb{E}_t \left\{ \begin{pmatrix} \sigma dB_t \\ d\eta_t \end{pmatrix} \begin{pmatrix} \sigma dB_t \\ d\eta_t \end{pmatrix}^\top \right\} = \begin{bmatrix} \mathbf{a} & \Sigma_{\eta, \sigma} \\ \Sigma_{\eta, \sigma}^\top & \Sigma_\eta \end{bmatrix} \quad (\text{A } 1)$$

492 . where, $d\eta_t = -\nabla(\sigma dB_t)^\top \mathbf{k}$, denotes the wave-vector stochastic forcing and, $\Sigma_\eta dt$, its
 493 covariance, and $\mathbb{E}_t \{\bullet\} \triangleq \mathbb{E} \{\bullet | \mathbf{x}_r(t), \mathbf{k}(t)\}$ stands for the conditional expectation evaluated
 494 with given characteristics $(\mathbf{x}_r(t), \mathbf{k}(t))$ at the current time t . Note that in the appendix we
 495 use Itô notations only.

496 The subgrid velocity, $\mathbf{v}' = \sigma dB_t/dt$ is constructed in Fourier space with a divergence-free
 497 isotropic spatial filter $\nabla^\perp \check{\psi}_\sigma$ (see (3.11)).

$$498 \quad \widehat{\mathbf{v}'}(\boldsymbol{\kappa}, t) = \int d\mathbf{x} \mathbf{v}'(\mathbf{x}, t) e^{-i\boldsymbol{\kappa} \cdot \mathbf{x}} = \widehat{\sigma dB_t/dt}(\boldsymbol{\kappa}, t) = i\boldsymbol{\kappa}^\perp \widehat{\check{\psi}}_\sigma(\boldsymbol{\kappa}) \widehat{dB_t}(\boldsymbol{\kappa})/dt, \quad (\text{A } 2)$$

499 where $\boldsymbol{\kappa}^\perp$ is the vector directly orthogonal to $\boldsymbol{\kappa}$. The computation of the variance tensor \mathbf{a}
 500 is classical and straightforward from the definition of the inverse Fourier transform and the
 501 identity $\mathbb{E} \left\{ \widehat{dB_t}(\boldsymbol{\kappa}_1) \widehat{dB_t}^*(\boldsymbol{\kappa}_2) \right\} = (2\pi)^2 \delta(\boldsymbol{\kappa}_1 - \boldsymbol{\kappa}_2) dt$, where $*$ denotes complex conjugate. We
 502 simply need to split the integral of the stochastic forcing spectrum over the current wavevector

503 $\boldsymbol{\kappa} = \kappa(\cos \theta_\kappa, \sin \theta_\kappa)$:

$$504 \quad \mathbf{a} = \frac{1}{(2\pi)^4 dt} \iint d\boldsymbol{\kappa}_1 d\boldsymbol{\kappa}_2 \mathbb{E}_t \left\{ (\widehat{\sigma dB_t})(\boldsymbol{\kappa}_1, \mathbf{k}) (\widehat{\sigma dB_t}^\top)^*(\boldsymbol{\kappa}_2, \mathbf{k}) \right\} e^{i(\boldsymbol{\kappa}_1 - \boldsymbol{\kappa}_2) \cdot \mathbf{x}}, \quad (\text{A } 3)$$

$$505 \quad = \frac{1}{(2\pi)^2} \int d\boldsymbol{\kappa} \kappa^2 |\widehat{\psi}_\sigma(\boldsymbol{\kappa})|^2 \begin{pmatrix} -\sin \theta_\kappa \\ \cos \theta_\kappa \end{pmatrix} \begin{pmatrix} -\sin \theta_\kappa \\ \cos \theta_\kappa \end{pmatrix}^\top, \quad (\text{A } 4)$$

$$506 \quad = \frac{1}{(2\pi)^2} \int_0^{+\infty} \oint_0^{2\pi} d\kappa d\theta_\kappa \kappa^3 |\widehat{\psi}_\sigma(\boldsymbol{\kappa})|^2 \begin{pmatrix} \sin^2 \theta_\kappa & -\sin \theta_\kappa \cos \theta_\kappa \\ -\sin \theta_\kappa \cos \theta_\kappa & \cos^2 \theta_\kappa \end{pmatrix}, \quad (\text{A } 5)$$

$$507 \quad = \frac{2}{2\pi} a_0 \oint_0^{2\pi} d\theta_\kappa \begin{pmatrix} \sin^2 \theta_\kappa & -\sin \theta_\kappa \cos \theta_\kappa \\ -\sin \theta_\kappa \cos \theta_\kappa & \cos^2 \theta_\kappa \end{pmatrix}, \quad (\text{A } 6)$$

$$508 \quad = a_0 \mathbb{I}_d, \quad (\text{A } 7)$$

509 where a_0 is defined by (4.7).

510 Now, the Fourier transform of the wave-vector stochastic forcing is

$$511 \quad d\widehat{\boldsymbol{\eta}}_t = -\nabla(\widehat{\sigma dB_t})^\top \mathbf{k} = -i\boldsymbol{\kappa}(i\boldsymbol{\kappa}^\perp \widehat{\psi}_\sigma \widehat{dB_t}) \cdot \mathbf{k} = \boldsymbol{\kappa}(\boldsymbol{\kappa}^\perp \cdot \mathbf{k}) \widehat{\psi}_\sigma \widehat{dB_t} = -\boldsymbol{\kappa}(\mathbf{k}^\perp \cdot \boldsymbol{\kappa}) \widehat{\psi}_\sigma \widehat{dB_t}. \quad (\text{A } 8)$$

512 Then, applying the crest-oriented rotation matrix, $\mathbf{M}_k = \begin{bmatrix} \tilde{\mathbf{k}} & \tilde{\mathbf{k}}^\perp \end{bmatrix}$, leads to

$$513 \quad d\widehat{\mathbf{Z}}_t = \mathbf{M}_k^\top d\widehat{\boldsymbol{\eta}}_t = -\begin{pmatrix} \tilde{\mathbf{k}} \cdot \boldsymbol{\kappa} \\ \tilde{\mathbf{k}}^\perp \cdot \boldsymbol{\kappa} \end{pmatrix} (\mathbf{k}^\perp \cdot \boldsymbol{\kappa}) \widehat{\psi}_\sigma \widehat{dB_t} = -\begin{pmatrix} \cos \delta\theta \sin \delta\theta \\ \sin^2 \delta\theta \end{pmatrix} \kappa^2 k \widehat{\psi}_\sigma \widehat{dB_t}, \quad (\text{A } 9)$$

514 with $\delta\theta = \theta_\kappa - \theta_k$. From there, we can evaluate the conditional covariance matrix $\Sigma_Z =$
515 $\frac{1}{dt} \mathbb{E}_t \{ d\mathbf{Z}_t d\mathbf{Z}_t^\top \}$ of $d\mathbf{Z}_t$ as before:

$$516 \quad \Sigma_Z = \frac{1}{(2\pi)^4 dt} \iint d\boldsymbol{\kappa}_1 d\boldsymbol{\kappa}_2 \mathbb{E}_t \left\{ (d\widehat{\mathbf{Z}}_t)(\boldsymbol{\kappa}_1, \mathbf{k}) (d\widehat{\mathbf{Z}}_t^\top)^*(\boldsymbol{\kappa}_2, \mathbf{k}) \right\} e^{i(\boldsymbol{\kappa}_1 - \boldsymbol{\kappa}_2) \cdot \mathbf{x}}, \quad (\text{A } 10)$$

$$517 \quad = \frac{1}{(2\pi)^2} \int_0^{+\infty} \oint_0^{2\pi} d\kappa d\delta\theta \kappa^5 k^2 |\widehat{\psi}_\sigma(\boldsymbol{\kappa})|^2 \begin{pmatrix} \cos^2 \delta\theta \sin^2 \delta\theta & \cos \delta\theta \sin^3 \delta\theta \\ \cos \delta\theta \sin^3 \delta\theta & \sin^4 \delta\theta \end{pmatrix} \quad (\text{A } 11)$$

$$518 \quad = \gamma_0 k^2 \begin{bmatrix} 1 & 0 \\ 0 & 3 \end{bmatrix}. \quad (\text{A } 12)$$

519 Finally, we come back to the canonical frame to get Σ_η

$$520 \quad \Sigma_\eta = \mathbb{E}_t \{ d\boldsymbol{\eta}_t d\boldsymbol{\eta}_t^\top \} = \mathbf{M}_k \Sigma_Z \mathbf{M}_k^\top = \gamma_0 k^2 \left[\tilde{\mathbf{k}} \tilde{\mathbf{k}}^\top + 3\tilde{\mathbf{k}}^\perp (\tilde{\mathbf{k}}^\perp)^\top \right]. \quad (\text{A } 13)$$

521 For noises cross-correlations, by isotropy, it is also straightforward to show that

$$522 \quad \Sigma_{\eta, \sigma} = 0. \quad (\text{A } 14)$$

523 The stochastic forcings of \mathbf{x}_r and \mathbf{k} are hence (conditionally) independent from one another.

524 Appendix B. Single ray dynamics

525 The Itô noise $\begin{pmatrix} \sigma dB_t \\ d\boldsymbol{\eta}_t \end{pmatrix}$ is white in time and conditionally Gaussian. Its conditional single-
526 point distribution is fully determined by its zero mean and its local covariance matrix (given
527 by equations (A 1), (A 7), (A 13) and (A 14)). In particular, we can replace this noise by
528 another zero-mean Gaussian vector with the same covariance without changing the single-

529 ray dynamics – typically replacing σdB_t by $\sqrt{a_0} \begin{pmatrix} dB_t^{(1)} \\ dB_t^{(2)} \end{pmatrix}$ and dZ_t by $-\sqrt{\gamma_0} k \begin{pmatrix} dB_t^{(3)} \\ \sqrt{3} dB_t^{(4)} \end{pmatrix}$. It
 530 yields the simplified ray equations (4.3)-(4.4).

531 Then note that from Itô lemma (Oksendal 1998) $d\tilde{\mathbf{k}} = d \begin{pmatrix} \cos \theta_k \\ \sin \theta_k \end{pmatrix} = \tilde{\mathbf{k}}^\perp d\theta_k - \frac{1}{2} \tilde{\mathbf{k}} d <$
 532 $\theta_k, \theta_k >_t$ where $< \bullet, \bullet >_t$ denotes the quadratic covariation. Thus,

$$533 \quad d\mathbf{k} = dk\tilde{\mathbf{k}} + kd\tilde{\mathbf{k}} + d < k, \tilde{\mathbf{k}} > = (dk - \frac{1}{2}kd < \theta_k, \theta_k >_t)\tilde{\mathbf{k}} + (kd\theta_k + d < k, \theta_k >_t)\tilde{\mathbf{k}}^\perp \quad (\text{B } 1)$$

534 Projecting this equation and $d\mathbf{k} = -\nabla\bar{\mathbf{v}}^\top \mathbf{k} dt + d\boldsymbol{\eta}_t$ on $\tilde{\mathbf{k}}$ and $\tilde{\mathbf{k}}^\perp$, we have

$$535 \quad \begin{cases} dk = -\tilde{\mathbf{k}} \cdot \nabla\bar{\mathbf{v}}^\top \mathbf{k} dt + (dZ_t)_1 + \frac{1}{2}kd < \theta_k, \theta_k >_t \\ kd\theta_k = -\tilde{\mathbf{k}}^\perp \cdot \nabla\bar{\mathbf{v}}^\top \mathbf{k} dt + (dZ_t)_2 - d < k, \theta_k >_t \end{cases}, \quad (\text{B } 2)$$

$$536 \quad \begin{cases} dk = -\tilde{\mathbf{k}} \cdot \nabla\bar{\mathbf{v}}^\top \mathbf{k} dt + (dZ_t)_1 + \frac{1}{2}k^{-1}d < Z_2, Z_2 >_t \\ d\theta_k = -\tilde{\mathbf{k}}^\perp \cdot \nabla\bar{\mathbf{v}}^\top \tilde{\mathbf{k}} dt + k^{-1}(dZ_t)_2 + \frac{1}{2}k^{-2}d < Z_1, Z_2 >_t \end{cases}. \quad (\text{B } 3)$$

537 The treatment of the large-scale terms $\tilde{\mathbf{k}} \cdot \nabla\bar{\mathbf{v}}^\top \tilde{\mathbf{k}}$ and $\tilde{\mathbf{k}}^\perp \cdot \nabla\bar{\mathbf{v}}^\top \tilde{\mathbf{k}}$ is classical. Interested
 538 readers can refer to Lapeyre *et al.* (1999) for details. From Ito lemma again, $d \log k =$
 539 $dk/k - \frac{1}{2}d < k, k >_t / k^2$ leading to the simplified wave-vector dynamics (4.5)-(4.6).

540 Appendix C. Subgrid flow anisotropy and comparison with other works

541 Throughout this paper, we have considered an isotropic model for the stochastic subgrid
 542 velocity (3.11). The isotropic diffusivity matrix $\mathbf{a} = a_0 \mathbb{I}_d$ is a good illustration of this. In
 543 contrast, many authors (e.g. White & Fornberg 1998; Bôas & Young 2020; Smit & Janssen
 544 2019) assume isotropic and homogeneous turbulence and obtain anisotropic stochastic
 545 subgrid models for $\frac{\|\mathbf{v}\|}{v_g^0} \rightarrow 0$. In these approaches, the integral over $\delta\theta$ in diffusivity matrix

546 computations (A 4) and (A 12) involve singular integrations over the direction $\mathbf{v}_g^0 = v_g^0 \tilde{\mathbf{k}}$. It
 547 makes appear a Dirac delta function, $2\pi\delta(\boldsymbol{\kappa} \cdot \mathbf{v}_g^0) = \frac{2\pi}{\kappa v_g^0} (\delta(\theta_\kappa - \theta_k - \frac{\pi}{2}) + \delta(\theta_\kappa - \theta_k + \frac{\pi}{2}))$

548 (see Appendix in Bôas & Young 2020). This precision imposes a statistical anisotropy for
 549 σdB_t (oriented along \mathbf{k}) and $d\boldsymbol{\eta}_t$ (oriented along \mathbf{k}^\perp), eventually leading to a covariance

$$550 \quad \Sigma_Z = \gamma_0 k^2 \begin{bmatrix} 0 & 0 \\ 0 & 16 \end{bmatrix} \quad (\text{Eq. (3.17) in Bôas \& Young (2020) and Eq. (24) in Smit \& Janssen$$

551 (2019)), no noise dZ_1 , and no Brownian motion $B_t^{(3)}$. Moreover, because of scaling
 552 assumption, Bôas & Young (2020) neglect the spatial diffusivity matrix, \mathbf{a} , while Smit
 553 & Janssen (2019) find $\mathbf{a} = 4a_0 \left(\mathbb{I}_d + \frac{5}{4} \tilde{\mathbf{k}} \tilde{\mathbf{k}}^\top \right)$ (Eq. (22)-(23)). In this anisotropic framework,
 554 the Stratonovich wavevector equation (2.3), $d\mathbf{k} = -\nabla(\bar{\mathbf{v}} dt + \sigma \circ dB_t)^\top \mathbf{k}$, would involve an
 555 additional drift term in Itô notations.

556 Further developing this anisotropic stochastic closure is an interesting avenue. A multiscale
 557 anisotropic stochastic closure would involve wavenumber variations but no wavenumber
 558 diffusion. Nevertheless, in the present study, we adopt the isotropic model for σdB_t , which
 559 is much more convenient for multi-ray numerical simulations.

560 Appendix D. Action spectra and ray distribution

561 Here we highlight the link between mean action spectral density and the ray distribution.
 562 We denote by N^0 the initial wave action spectrum. We first use the definition of the Dirac

563 measure then we perform a variable change corresponding to the characteristic (2.5) from
564 $t = t_i$ to $t = t_f$:

$$565 \quad \mathbb{E}N(\mathbf{x}, \mathbf{k}, t) = \mathbb{E} \iint d\mathbf{x}_r d\mathbf{k}_r N(\mathbf{x}_r, \mathbf{k}_r, t) \delta(\mathbf{x}_r - \mathbf{x}) \delta(\mathbf{k}_r - \mathbf{k}), \quad (\text{D } 1)$$

$$566 \quad = \mathbb{E} \iint d\mathbf{x}_r^0 d\mathbf{k}_r^0 N(\mathbf{x}_r^0, \mathbf{k}_r^0, 0) \delta(\mathbf{x}_r(\mathbf{x}_r^0, \mathbf{k}_r^0, t) - \mathbf{x}) \delta(\mathbf{k}_r(\mathbf{x}_r^0, \mathbf{k}_r^0, t) - \mathbf{k}), \quad (\text{D } 2)$$

$$567 \quad = \iint d\mathbf{x}_r^0 d\mathbf{k}_r^0 N^0(\mathbf{x}_r^0, \mathbf{k}_r^0) p(\mathbf{x}, \mathbf{k} | \mathbf{x}_r^0, \mathbf{k}_r^0, t), \quad (\text{D } 3)$$

568 where the standard relation between the Dirac measure and the probability distribution
569 function has been used.

570 Appendix E. Jet simulation

571 Again, currents are simulated at a resolution 512×512 on a 1000-km-width squared domain
572 $[0, L_x] \times [0, L_y]$ through the same code. A backward velocity v_{Bk} forces a leftward jet
573 structure.

$$574 \quad \partial_t \omega + \mathbf{v} \cdot \nabla \omega = S_\omega \quad \text{with} \quad \mathbf{v} = \nabla^\perp \Delta^{-1}(\omega + \omega_{\text{Bk}}). \quad (\text{E } 1)$$

575 S_ω encompasses the linear drag and the hyperviscosity with coefficient $1/\tau_F = 3.22 \times 10^{-8} s^{-1}$
576 and $\nu_{\text{HV}}/dx^8 = 3.33 \times 10^{-9} s^{-1}$ respectively. The background vorticity, ω_{Bk} , is a smooth step
577 function with a wavy interface at $y = Y_{\text{Bk}}(x)$:

$$578 \quad \omega_{\text{Bk}}(x, y) = \Omega_{\text{Bk}} \left(\frac{1}{2} - \text{erf} \left(\frac{y - Y_{\text{Bk}}(x)}{L_y^\omega} \right) \right) \quad \text{with} \quad Y_{\text{Bk}}(x) = L_y \left(\frac{1}{2} + \frac{1}{30} \cos \left(\frac{2\pi x}{L_x} \right) \right). \quad (\text{E } 2)$$

579 To better highlight the interplay between ray oscillations and scattering, we consider
580 very-collimated swells, with a spatial extension of $100\lambda = 25$ km.

581 Besides, the curvature of the simulated jet can force an additional faster oscillation around
582 the jet for small enough wavevector angle. Indeed, a wave group traveling exactly rightward
583 would cross an alternation of positive and negative vorticity regions with a period $L_x/(v_g^0 -$
584 $\bar{U}_0) \approx 1$ day $< 2\pi/\bar{\omega}_r$. Here, we set an initial wavevector angle large enough to prevent the
585 additional harmonics.

REFERENCES

- 586 BAL, GUILLAUME & CHOU, TOM 2002 Capillary–gravity wave transport over spatially random drift. *Wave*
587 *Motion* **35** (2), 107–124.
- 588 BAUER, WERNER, CHANDRAMOULI, PRANAV, CHAPRON, BERTRAND, LI, LONG & MÉMIN, ETIENNE 2020
589 Deciphering the role of small-scale inhomogeneity on geophysical flow structuration: a stochastic
590 approach. *Journal of Physical Oceanography* **50** (4), 983–1003.
- 591 BÔAS, ANA B VILLAS & YOUNG, WILLIAM R 2020 Directional diffusion of surface gravity wave action by
592 ocean macroturbulence. *Journal of Fluid Mechanics* **890**.
- 593 BORCEA, LILIANA, GARNIER, JOSSELYN & SOLNA, KNUT 2019 Wave propagation and imaging in moving
594 random media. *Multiscale Modeling & Simulation* **17** (1), 31–67.
- 595 BOURY, SAMUEL, BÜHLER, OLIVER & SHATAH, JALAL 2023 Fast-slow wave transitions induced by a random
596 mean flow. *Physical Review E* **108** (5), 055101.
- 597 BÜHLER, OLIVER 2009 *Waves and mean flows*. Cambridge University Press.
- 598 COTTER, COLIN J, GOTTWALD, GEORG A & HOLM, DARRYL D 2017 Stochastic partial differential fluid
599 equations as a diffusive limit of deterministic lagrangian multi-time dynamics. *Proceedings of the*
600 *Royal Society A: Mathematical, Physical and Engineering Sciences* **473** (2205), 20170388.

- 601 COX, MICHAEL R, KAFIABAD, HOSSEIN A & VANNESTE, JACQUES 2023 Inertia-gravity-wave diffusion by
602 geostrophic turbulence: the impact of flow time dependence. *Journal of Fluid Mechanics* **958**, A21.
- 603 CRISAN, DAN & HOLM, DARRYL D 2018 Wave breaking for the stochastic camassa–holm equation. *Physica*
604 *D: Nonlinear Phenomena* **376**, 138–143.
- 605 DINVAY, EVGUENI & MÉMIN, ETIENNE 2022 Hamiltonian formulation of the stochastic surface wave problem.
606 *Proceedings of the Royal Society A* **478** (2265), 20220050.
- 607 DONG, WENJING, BÜHLER, OLIVER & SMITH, K SHAFER 2020 Frequency diffusion of waves by unsteady
608 flows. *Journal of Fluid Mechanics* **905**, R3.
- 609 DYSTHE, KRISTIAN B 2001 Refraction of gravity waves by weak current gradients. *Journal of Fluid Mechanics*
610 **442**, 157–159.
- 611 FREUND, JB & FLEISCHMAN, TG 2002 Ray traces through unsteady jet turbulence. *International Journal of*
612 *Aeroacoustics* **1** (1), 83–96.
- 613 GARNIER, JOSSELIN, GAY, ETIENNE & SAVIN, ERIC 2020 Multiscale analysis of spectral broadening of acoustic
614 waves by a turbulent shear layer. *Multiscale Modeling & Simulation* **18** (2), 798–823.
- 615 HELD, I., PIERREHUMBERT, R., GARNER, S. & SWANSON, K. 1995 Surface quasi-geostrophic dynamics.
616 *Journal of Fluid Mechanics* **282**, 1–20.
- 617 HELL, MOMME C, FOX-KEMPER, BAYLOR & CHAPRON, BERTRAND in preparation An efficient wave model for
618 surface wave growth and propagation in coupled climate models. *Journal of Advances in Modeling*
619 *Earth Systems* .
- 620 HELLER, EJ, KAPLAN, L & DAHLEN, A 2008 Refraction of a gaussian seaway. *Journal of Geophysical*
621 *Research: Oceans* **113** (C9).
- 622 HOLM, D. 2015 Variational principles for stochastic fluid dynamics. *Proceedings of the Royal Society of*
623 *London A: Mathematical, Physical and Engineering Sciences* **471** (2176).
- 624 HOLM, DARRYL D 2021 Stochastic variational formulations of fluid wave–current interaction. *Journal of*
625 *nonlinear science* **31** (1), 4.
- 626 HOLM, DARRYL D, HU, RUIAO & STREET, OLIVER D 2023 On the interactions between mean flows and
627 inertial gravity waves. *arXiv preprint arXiv:2302.04838* .
- 628 HOLM, DARRYL D & LUESINK, ERWIN 2021 Stochastic wave–current interaction in thermal shallow water
629 dynamics. *Journal of Nonlinear Science* **31**, 1–56.
- 630 JONSSON, IVAR G 1990 Wave-current interactions. *The sea* **9**, 65–120.
- 631 KAFIABAD, HOSSEIN A, SAVVA, MILES AC & VANNESTE, JACQUES 2019 Diffusion of inertia-gravity waves
632 by geostrophic turbulence. *Journal of Fluid Mechanics* **869**, R7.
- 633 KLYATSKIN, V. 2005 *Stochastic equations through the eye of the physicist: Basic concepts, exact results and*
634 *asymptotic approximations*. Elsevier.
- 635 KLYATSKIN, VI & KOSHEL, KV 2015 Anomalous sea surface structures as an object of statistical topography.
636 *Physical Review E* **91** (6), 063003.
- 637 KUDRYAVTSEV, VLADIMIR, YUROVSKAYA, MARIA, CHAPRON, BERTRAND, COLLARD, FABRICE & DONLON,
638 CRAIG 2017 Sun glitter imagery of ocean surface waves. part 1: Directional spectrum retrieval and
639 validation. *Journal of Geophysical Research: Oceans* **122** (2), 1369–1383.
- 640 KUNITA, H. 1997 *Stochastic flows and stochastic differential equations*, , vol. 24. Cambridge university press.
- 641 LANDAU, LEV DAVIDOVICH & LIFSHITS, EVGENĪ MIKHAĬLOVICH 1960 *Mechanics*, , vol. 1. CUP Archive.
- 642 LAPEYRE, GUILLAUME 2017 Surface quasi-geostrophy. *Fluids* **2** (1), 7.
- 643 LAPEYRE, G., KLEIN, P. & HUA, B. 1999 Does the tracer gradient vector align with the strain eigenvectors in
644 2D turbulence? *Physics of Fluids* **11** (12), 3729–3737.
- 645 LAVRENOV, IGOR 2013 *Wind-waves in oceans: dynamics and numerical simulations*. Springer Science &
646 Business Media.
- 647 MCCOMAS, C HENRY & BRETHERTON, FRANCIS P 1977 Resonant interaction of oceanic internal waves.
648 *Journal of Geophysical Research* **82** (9), 1397–1412.
- 649 MÉMIN, E. 2014 Fluid flow dynamics under location uncertainty. *Geophysical & Astrophysical Fluid*
650 *Dynamics* **108** (2), 119–146.
- 651 MÉMIN, ETIENNE, LI, LONG, LAHAYE, NOÉ, TISSOT, GILLES & CHAPRON, BERTRAND 2022 Linear wave
652 solutions of a stochastic shallow water model. In *Stochastic Transport in Upper Ocean Dynamics*
653 *Annual Workshop*, pp. 223–245. Springer Nature Switzerland Cham.
- 654 MIKULEVICIUS, R. & ROZOVSKII, B. 2004 Stochastic Navier–Stokes equations for turbulent flows. *SIAM*
655 *Journal on Mathematical Analysis* **35** (5), 1250–1310.
- 656 OKSENDAL, B. 1998 *Stochastic differential equations*. Springer-Verlag.

- 657 PAPANICOLAOU, G. & KOHLER, W. 1974 Asymptotic theory of mixing stochastic ordinary differential
658 equations. *Communications on Pure and Applied Mathematics* **27** (5), 641–668.
- 659 PITERBARG, LEONID & OSTROVSKII, A 1997 *Advection and diffusion in random media: implications for sea*
660 *surface temperature anomalies*. Kluwer Academic.
- 661 PLOUGONVEN, RIWAL & ZHANG, FUQING 2014 Internal gravity waves from atmospheric jets and fronts.
662 *Reviews of Geophysics* **52** (1), 33–76.
- 663 RESSEGUIER, VALENTIN, LI, LONG, JOUAN, GABRIEL, DÉRIAN, PIERRE, MÉMIN, ETIENNE & BERTRAND,
664 CHAPRON 2020a New trends in ensemble forecast strategy: uncertainty quantification for coarse-grid
665 computational fluid dynamics. *Archives of Computational Methods in Engineering* pp. 1–82.
- 666 RESSEGUIER, VALENTIN, MÉMIN, ETIENNE & CHAPRON, BERTRAND 2017a Geophysical flows under location
667 uncertainty, part I random transport and general models. *Geophysical & Astrophysical Fluid*
668 *Dynamics* **111** (3), 149–176.
- 669 RESSEGUIER, VALENTIN, MÉMIN, ETIENNE & CHAPRON, BERTRAND 2017b Geophysical flows under location
670 uncertainty, part II quasi-geostrophy and efficient ensemble spreading. *Geophysical & Astrophysical*
671 *Fluid Dynamics* **111** (3), 177–208.
- 672 RESSEGUIER, VALENTIN, PAN, WEI & FOX-KEMPER, BAYLOR 2020b Data-driven versus self-similar
673 parameterizations for stochastic advection by lie transport and location uncertainty. *Nonlinear*
674 *Processes in Geophysics* **27** (2), 209–234.
- 675 SLUNYAEV, AV & SHRIRA, VI 2023 Extreme dynamics of wave groups on jet currents. *Physics of Fluids*
676 **35** (12).
- 677 SMIT, PB, HOUGHTON, IA, JORDANOVA, K, PORTWOOD, T, SHAPIRO, E, CLARK, D, SOSA, M & JANSSEN, TT
678 2021 Assimilation of significant wave height from distributed ocean wave sensors. *Ocean Modelling*
679 **159**, 101738.
- 680 SMIT, PIETER B & JANSSEN, TIM T 2019 Swell propagation through submesoscale turbulence. *Journal of*
681 *Physical Oceanography* **49** (10), 2615–2630.
- 682 VORONOVICH, A. 1991 The effect of shortening of waves on random currents. In *Proceedings of nonlinear*
683 *water waves*. Bristol.
- 684 WANG, HAN, BÔAS, ANA B VILLAS, YOUNG, WILLIAM R & VANNESTE, JACQUES 2023 Scattering of swell by
685 currents. *arXiv preprint arXiv:2305.12163* .
- 686 WEST, BRUCE J 1978 Ray paths in a fluctuating environment. *Physical Review A* **18** (4), 1646.
- 687 WHITE, BENJAMIN S 1999 Wave action on currents with vorticity. *Journal of Fluid Mechanics* **386**, 329–344.
- 688 WHITE, BENJAMIN S & FORNBERG, BENGT 1998 On the chance of freak waves at sea. *Journal of fluid*
689 *mechanics* **355**, 113–138.
- 690 ZHEN, YICUN, RESSEGUIER, VALENTIN & CHAPRON, BERTRAND 2023 Physically constrained covariance
691 inflation from location uncertainty. *EGUsphere* **2023**, 1.